Edith Cowan University

Research Online

Research outputs 2022 to 2026

7-1-2023

Liquefaction proneness of stratified sand-silt layers based on cyclic triaxial tests

Arpit Jain

Satyendra Mittal

Sanjay Kumar Shukla
Edith Cowan University

Follow this and additional works at: https://ro.ecu.edu.au/ecuworks2022-2026

 Part of the Civil and Environmental Engineering Commons

10.1016/j.jrmge.2022.09.015
Jain, A., Mittal, S., & Shukla, S. K. (2023). Liquefaction proneness of stratified sand-silt layers based on cyclic triaxial tests. Journal of Rock Mechanics and Geotechnical Engineering, 15(7), 1826-1845. https://doi.org/10.1016/j.jrmge.2022.09.015
This Journal Article is posted at Research Online.
https://ro.ecu.edu.au/ecuworks2022-2026/2562

Journal of Rock Mechanics and Geotechnical Engineering 15 (2023) 1826–1845

Contents lists available at ScienceDirect

Journal of Rock Mechanics and Geotechnical Engineering

journal homepage: www.jrmge.cn

Full Length Article

Liquefaction proneness of stratified sand-silt layers based on cyclic triaxial tests

Arpit Jain [a,*], Satyendra Mittal [a], Sanjay Kumar Shukla [b,c,d]

[a] Department of Civil Engineering, Indian Institute of Technology, Roorkee, Uttarakhand, India
[b] School of Engineering, Edith Cowan University, Joondalup, Perth, Australia
[c] Department of Civil Engineering, Indian Institute of Technology Madras, Chennai, India
[d] Department of Civil Engineering, BIT Sindri, India

ARTICLE INFO

Article history:
Received 10 June 2022
Received in revised form
26 July 2022
Accepted 15 September 2022
Available online 5 November 2022

Keywords:
Cyclic triaxial tests
Soil stratification
Soil liquefaction
Regression model

ABSTRACT

Most studies on liquefaction have addressed homogeneous soil strata using sand or sand with fine content without considering soil stratification. In this study, cyclic triaxial tests were conducted on the stratified sand specimens embedded with the silt layers to investigate the liquefaction failures and void-redistribution at confining stress of 100 kPa under stress-controlled mode. The loosening of underlying sand mass and hindrance to pore-water flow caused localized bulging at the sand-silt interface. It is observed that at a silt thickness of 0.2H (H is the height of the specimen), nearly 187 load cycles were required to attain liquefaction, which was the highest among all the silt thicknesses with a single silt layer. Therefore, 0.2H is assumed as the optimum silt thickness (t_{opt}). The silt was placed at the top, middle and bottom of the specimen to understand the effect of silt layer location. Due to the increase in depth of the silt layer from the top position (capped soil state) to the bottom, the cycles to reach liquefaction ($N_{cyc,L}$) increased 2.18 times. Also, when the number of silt layers increased from single to triple, there was an increase of about 880% in $N_{cyc,L}$. The micro-characterization analysis of the soil specimens indicated silty materials transported in upper sections of the specimen due to the dissipated pore pressure. The main parameters, including thickness (t), location (z), cyclic stress ratio (CSR), number of silt layers (n) and modified relative density ($D_{r,m}$), performed significantly in governing the liquefaction resistance. For this, a multilinear regression model is developed based on critical parameters for prediction of $N_{cyc,L}$. Furthermore, the developed constitutive model has been validated using the data from the present study and earlier findings.

© 2023 Institute of Rock and Soil Mechanics, Chinese Academy of Sciences. Production and hosting by Elsevier B.V. This is an open access article under the CC BY-NC-ND license (http://creativecommons.org/licenses/by-nc-nd/4.0/).

1. Introduction

During the earthquakes of Niigata (in 1964), Christchurch (in 2014), Bhuj (in 2001) and Assam (in 2021), the development of large excess pore pressure was responsible for the liquefaction failures. Liquefaction of freshwater carbonates in the vicinity of Çollar Coal-field was responsible for the loss of several lives due to geological instability (e.g. Akçar et al., 2019). In a modern approach, Guan et al. (2022) utilized the adaptive sampling technique for characterizing spatial distribution to calculate the liquefaction susceptibility of soil after performing cone-penetration tests. Previous studies on soil liquefaction mainly used homogeneous soil or with a certain amount of fine content, which may result in oversimplification of liquefaction-related failures or underestimation of resistance developed due to stratification. However, liquefaction failures nearby tailing dams, alluvial or marine deposits require a clear understanding of stratified or layered soil systems (e.g. Elgamal et al., 1989; Kokusho and Fujita, 2001; Kokusho and Kojima, 2002). The liquefaction potential of several sites nearby hydraulic fills or marine structures is significantly affected by the presence of stratified sandy strata interlayered with patches of silty soil. Researchers (e.g. Bucci et al., 2018; Norini, 2021; Woźniak et al., 2021) observed the potential triggering of liquefaction phenomenon nearby alluvial plains, dune environment, marine conditions and coastal sediments. The geological characteristics of impermeable silt seam were responsible for the sand boiling phenomenon, lateral spreading and significant settlements in stratified soil (e.g. Liu and Qiao, 1984; Balakrishnan and Kutter, 1999). In the centrifuge experiments performed by

* Corresponding author.
E-mail address: ajain4@ce.iitr.ac.in (A. Jain).
Peer review under responsibility of Institute of Rock and Soil Mechanics, Chinese Academy of Sciences.

https://doi.org/10.1016/j.jrmge.2022.09.015
1674-7755 © 2023 Institute of Rock and Soil Mechanics, Chinese Academy of Sciences. Production and hosting by Elsevier B.V. This is an open access article under the CC BY-NC-ND license (http://creativecommons.org/licenses/by-nc-nd/4.0/).

Fiegel and Kutter (1994), stratification was developed using fine sand blanketed by silica flour with less permeability. The excess pore pressure dissipated through the weakest portion of silica flour indicated a high probability of lateral spreading and liquefaction failures under stratification conditions. A similar observation was obtained due to the stratification and inhomogeneity in the permeability of the soil (e.g. Arulanandan and Scott, 1993; Balakrishnan and Kutter, 1999). The stiffness of an underlying clay layer has been responsible for the liquefaction-based failures in the reclaimed ground (Yamaguchi et al., 2002). The clay layer was conducted at different degrees of consolidation to simulate soil behaviors during the Hyogoken-Nambu earthquake. Kulasingam et al. (2004) conducted a series of centrifuge tests on the homogeneous and silt interlayered stratified specimens and observed the phenomenon of void redistribution and strain localization in the underlying liquefiable sandy strata. The analysis was carried out at varying shaking intensities, variable silt locations and different relative densities to obtain a clear understanding of the liquefaction failures nearby slopes with silt interlayers. Malvick et al. (2005) performed 1g model tests and centrifuge tests to assess the shear deformations, void-redistribution and water film development in the layered soil strata. The liquefaction triggering of stratified deposits significantly contributes to lateral spreading and flow slides.

Brennan and Madabhushi (2005) conducted dynamic centrifuge tests on the capped and stratified soil system prepared using less permeable rock flour and fine sand to recreate the geological environment near marine or alluvial plains. Using one-dimensional (1D) shaking table tests, Özener et al. (2009) established a useful correlation between excess pore water pressure, relative density, and input acceleration after interlayering sand deposits with a less permeable silt seam. Maharjan and Takahashi (2013) developed the soil stratification using patches of silt layers in sandy soil and noticed the significant changes in the permeability of soil strata using centrifuge tests. However, due to the enormous pore pressures and restricted pore water movement, uneven settlements were quite common. Lee et al. (2014) performed several centrifuge tests to investigate the seismic behaviors of sand with intra-silt layers. They observed the key changes in the rate of pore pressure dissipation and settlement of the strata due to a less permeable intra-silt layer. To closely observe the failures that occurred during the Christchurch earthquake, Markham et al. (2018) performed cyclic triaxial tests on the soil obtained from the earthquake-damaged shallow foundation. A comparative analysis has been discussed based on the field results and laboratory outcomes. Tasiopoulou et al. (2019) investigated the behaviors of undisturbed soil specimens with clay laminates using cyclic triaxial testing and numerical models (developed through FLAC^{2D}). The authors observed the absence of strain localization inside the existing sand layers in the presence of the clay laminates, which were responsible for the enhancement of liquefaction resistance. Karakan et al. (2019a) considered cyclic triaxial tests to understand the behavior of silty soil (with pore pressure ratios less than 50%). Limited liquefaction was observed due to the changes in silt volume caused by the reconsolidation under cyclic loadings. Erdoğan et al. (2020) utilized a modern cluster algorithm to assess the liquefaction susceptibility of non-plastic silt after using the data obtained from 54 cyclic triaxial tests. The results suggest that the unsupervised cluster algorithms are valuable tools to investigate liquefaction and post-liquefaction induced by volumetric strains. Ecemis (2021) scrutinized the seismic behavior of non-homogeneous stratified soil using shaking table models and numerical analysis. The author suggested that the thickness of the silt seam has a major influence on the liquefaction susceptibility of stratified sand deposits. Due to liquefaction, soil exhibit a considerable amount of stiffness degradation, which can be optimally investigated using cyclic triaxial after carefully observing the development of pore pressure. Ni et al. (2022) performed undrained cyclic triaxial tests on sandy soil to formulate an empirical correlation between pore pressure developed in the first loading cycle and the number of failure cycles to attain liquefaction. Wang et al. (2020) performed a series of static-dynamic triaxial tests on the saturated gravelly soil to investigate the pre- and post-liquefaction phenomenon, in addition to the micro-parameters of the granular soil systems.

To understand the liquefaction phenomenon of stratified specimens, it is essential to scrutinize pore pressure in each participating layer (sand or silt). The behavior of non-plastic silt is entirely different from that of the sandy soil, therefore, Karakan et al. (2019b) performed the cyclic triaxial tests on non-plastic silty specimens to observe the pore pressure variation and axial strain during liquefaction and post-liquefaction conditions. Kumar et al. (2018) investigated the liquefaction behavior of cohesive soil after applying staged cyclic loadings, and calculated the dynamic properties of cohesive soil. After performing several stress-controlled cyclic triaxial tests, Karakan and Altun (2018) observed the liquefaction behaviors of sandy specimens with varying silt contents. The authors suggested the key changes in pore pressure development and failure mechanism due to silt particles in the sandy skeleton. There is a limited investigation of silt interlayered sandy specimens using cyclic triaxial tests, where a cyclic loading triggers the development of crucial excess pore pressures (e.g. Jia and Bingye, 2012; Xiu et al., 2019) leading to the cyclic mobility failures. In these studies, there exists an optimum silt layer thickness, at which liquefaction resistance is maximum in the silt interlayered specimens. After performing several strain-controlled cyclic triaxial tests, Xiu et al. (2019) concluded that the susceptibility towards liquefaction was found to be the highest when the less permeable silt was located nearer to the top of the specimen. Jain et al. (2022) investigated the crucial role of silt layer depth after applying cyclic loadings on the silt interlayered sandy specimens. The authors suggested that the specimen having silt layer closer to the top emerged as most vulnerable to liquefaction initiation.

The environmental circumstances nearby marine deposits, alluvial sites and hydraulic fills have a stratum with silt interlayering, lying at different depths and thicknesses. Most previous findings on liquefaction-induced failures neglect the role of silt-interlayers or patches of less permeable soil. Limited investigations on the liquefaction triggering of silt-interlayered sandy specimens have been attempted to replicate the real soil conditions. These studies also fail to demonstrate the development of localized pore pressure, induced bulging, or any analytical development. In this study, investigation of the dynamic behaviors of stratified specimens is presented based on extensive cyclic triaxial testing, micro characterization, and regression models. Shear modulus is used to assess the changes in stiffness characteristics after using silt interlayers. The obtained results indicate the critical role of silt layer parameters, i.e. thickness (t), location (z), and number of silt layers (n). Additionally, multi-linear regression models have been developed to anticipate the cycles required to attain liquefaction ($N_{cyc,L}$) using silt layer parameters, relative density, and cyclic stress ratio (CSR), with satisfactory validations.

2. Experimental details

2.1. Materials

In this study, Solani River sand (fine sand) and pure silt were used as the testing materials. The sandy soil was collected from the bed of the Solani River and silt was collected from the bank of the canal located near Solanipuram Park, Roorkee, India. This Roorkee region lies in the seismic zone IV, therefore, a liquefaction study is quite useful in understanding vulnerability of the area (e.g. Kirar

and Maheshwari, 2018; Jain et al., 2021). Previously, materials with low permeability (4×10^{-6} m/s), such as rock flour (e.g. Brennan and Madabhushi, 2005), powdery material (e.g. Xiu et al., 2019) and silt (e.g. Konrad and Dubeau, 2003) were used in the stratified specimens. Therefore, in this study, low permeable silty soil used by previous researchers has been chosen. After cyclic loads, the non-plastic silt particles can also liquefy due to loss of shear strength. A similar phenomenon was proposed by Xu et al. (2016) under the action of sea waves, where the silt sediments depicted significant liquefaction which led to convoluted, parallel and graded bedding. The grain size distribution curve is presented in Fig. 1 for both materials. The physical properties of them have been calculated as per IS 2720-4 (1985) and are presented in Tables 1 and 2.

In this study, scanning electron microscopic (SEM) images were used to capture the shape of Solani River sand and silt (× 500). The methodology adopted by Ghadr and Assadi-Langroudi (2019) was utilized in the present work to investigate the shape characteristics. Several parts of the Solani River sand and silt were randomly selected, in which a total of 50-grain particles were considered using the SEM images shown in Fig. 2.

The characteristics of particle shape have been evaluated for the random set of soil grains as described below:

(i) Sphericity (r_s)

This parameter facilitates an understanding of the degree of convergence presented in a three-dimensional (3D) coordinate system with the help of dimensions of particles:

$$r_s = \frac{r_{max-in}}{r_{min-cir}} \quad (1)$$

where $r_{max\text{-}in}$ is radius of the largest sphere inscribing particle, which can be termed as the equivalent particle radius; $r_{min\text{-}cir}$ is radius of the smallest sphere circumscribing the particle.

(ii) Roundness (r_r)

It is the equivalent average radius of surficial characteristics:

$$r_r = \frac{\sum \frac{r_i}{N}}{r_{max-in}} \quad (2)$$

where r_i is the equivalent average radius of surficial features, and N is the number of particles.

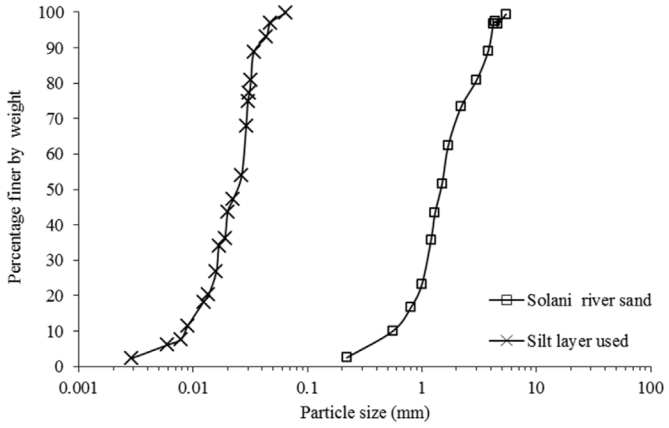

Fig. 1. Particle size distribution.

Table 1
Physical properties of Solani River sand.

Parameter	Value
Mean particle size, D_{50}	0.2 mm
Coefficient of uniformity, C_u	1.95
Specific gravity, G_s	2.65
Maximum void ratio, e_{max}	0.88
Minimum void ratio, e_{min}	0.57
Permeability, k	7.2×10^{-3} cm/s

Table 2
Physical properties of silt.

Property	Notation	Value
Soil type	Low plastic silt	–
Mean particle size	D_{50}	0.017 mm
Specific gravity	G_s	2.68
Maximum void ratio	e_{max}	1.27
Minimum void ratio	e_{min}	0.34
Liquid limit	w_l	15%
Plastic limit	w_p	12%
Permeability	k	5.8×10^{-5} cm/s

The geometrical properties of Solani River sand and silt can be calculated. For Solani River sand: $r_s = 0.88$ and $r_r = 0.97$. For silt: $r_s = 0.65$ and $r_r = 0.45$. Therefore, Solani River sand and silt can be considered as sub-rounded and angular, respectively.

2.2. Cyclic triaxial testing apparatus

Stress-controlled cyclic triaxial tests were performed as per ASTM D5311 (2013) under consolidated undrained conditions using pneumatically controlled cyclic triaxial testing apparatus. The apparatus can be enabled in both load-controlled and displacement-controlled modes as per the testing requirements at a frequency ranging from 0.1 Hz to 10 Hz, with a maximum loading capacity of 50 kN. Several loading patterns like sinusoidal, impact, triangular and square can be applied to the specimens. To ascertain the accuracy of load imposed on the specimen, a specially designed load cell with a sensitivity of 0.1% was placed inside the chamber to avoid friction coming due to the connecting rod. The calculation of developed strains is possible through the linearly variable differential transducers (LVDT) with a maximum range of ±50 mm. Also, pore pressure can be measured through the pore pressure transducers (PPT) with a maximum capacity of 2000 kPa. Specimens with 70 mm diameter (D) and 140 mm height (H) were considered in the study.

2.3. Methodology

A total of 47 stress-controlled cyclic triaxial tests were performed in the study (see Table 3). Additionally, four strain-controlled tests have been performed for calculation of the shear modulus. Each test was performed three times to ascertain the accuracy. Firstly, after applying a vacuum inside the mold, the latex membrane was stretched inside. Special care was taken while preparing stratified specimens, therefore, suitable demarcation lines were drawn in accordance with the desired thickness, density and location, as shown in Fig. 3. Then, a pre-calculated amount of material was poured inside the mold using a suitable specimen preparation technique. Uniform compaction was provided using a tamping rod. The specimen preparation is shown in Fig. 3d and e. In order to ensure optimum compaction, marking was used and checked using a scale. This confirmed that the pre-calculated amount of soil had been placed between the desired markings to

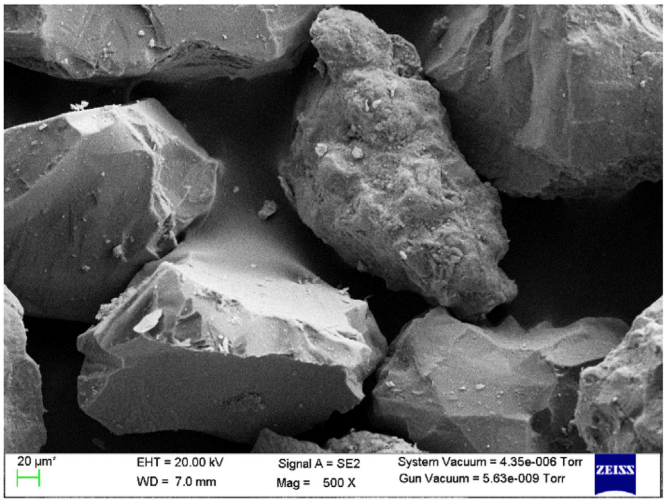

(a)

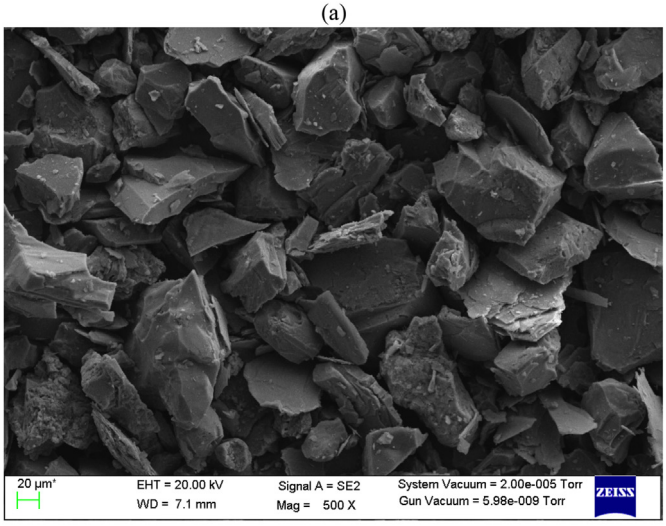

(b)

Fig. 2. SEM images of the materials used: (a) Solani River sand and (b) Silt.

achieve actual density. The stratified specimens were prepared using the air pluviation technique under slight tamping. Homogeneous sand and stratified specimens were prepared using the air pluviation technique with slight tamping, whereas pure silt specimens were prepared using the moist tamping method (e.g. Singh, 1996). Due to the small particle size of silt, the pure silt specimens cannot be effectively prepared using the air pluviation technique because these particles would fall outside the mold. Therefore, two different specimen preparation techniques were adopted for preparation of sand and silt. Karakan et al. (2019a) also adopted the wet tamping technique for preparation of silty specimens. Homogeneous specimens were prepared in five different layers and stratified specimens were prepared in seven layers. The tests have been performed after varying the relative densities of sand (i.e. 29.62%–50.48%) and silt (i.e. 30.08%–72.85%) layers which directly help in understanding the liquefaction failures in the stratified soil systems of sand-silt deposits (Table 3). The testing was based on cyclic triaxial and it was not possible to use silt layer paste in the formation of the stratified specimen. The reason behind this was the improper flow of carbon-dioxide, which governs the optimum saturation of the whole specimen. Therefore, the density of the silt layer appeared to be a significant parameter in governing liquefaction. The chosen density of the silt layer developed a significant blockage in internal movement of pore-water flow through the specimen; consequently, silt was placed at a relative density of 30.08%–72.85%. The density of a stratified specimen seems to be different from that of the individual soil or homogeneous layer. Due to this, the overall density of the stratified specimen cannot be considered without proper formulation. Therefore, Yoshimine and Koike (2005) suggested the following equations for modified density in stratified cases, which were also adopted by Xiu et al. (2019) and Jia and Bingye (2012):

$$D_{r,m} = \frac{e_{max,m} - e}{e_{max,m} - e_{min,m}} \tag{3}$$

$$e_{max,m} = \sum \left[R_{m,i} \left(e_{max,i} + 1 \right) \right] - 1 \tag{4}$$

$$e_{min,m} = \sum \left[R_{m,i} \left(e_{min,i} + 1 \right) \right] - 1 \tag{5}$$

where $e_{min,m}$, $e_{max,m}$, $D_{r,m}$ and $R_{m,i}$ are the modified minimum void ratio, modified maximum void ratio, modified relative density and percentage of the dry weight of ith layer in the stratified soil, respectively. Table 4 shows the details of $D_{r,m}$, $e_{max,m}$, and $e_{min,m}$ for all the specimens. On account of the inability of sand and silt specimens to stand vertical on their own, initially the vacuum was applied to the specimen before applying a confining pressure of about 40 kPa to avoid any lateral movement. We used the solubility advantage of carbon dioxide in water, followed by water flushing. Then, with the advancement of 20 kPa in both back and confining pressure, the Skempton's pore pressure coefficient (B value) was achieved (>0.98) for completion of the saturation process. Furthermore, the consolidation was performed on the specimen at a confining pressure of 100 kPa. In this study, it was noticed that the time required for consolidation (t_{conso}) changes with the thickness of silt layer but a marginal difference is noticed for the changes in the location of the silt layer (Table 5). The values of t_{conso} for the tested specimens are presented in Table 5. As the thickness of silt layer increased from 0 to 0.4H or (0–56 mm), the time required for consolidation also increased. The reason was the mobility of water molecules which became slow with an increase in silt thickness. Although there was a marginal difference in t_{conso} for specimens with different silt layer locations, it has been observed that the specimen with silt layer at higher depth was consolidated lately. This is due to the bottom location of the back pressure valve which allows the volume to change from the upper to lower portion of the specimen (Fig. 3e). In Fig. 3e, red arrows depict the movement of water molecules. Additionally, when the number of silt layers increased from 0 to 3, there was a significant increase in t_{conso}. The time required for consolidation rose by 2.1 times when the number of silt layers increased from single (specimen 9) to triple (specimen S15). After consolidation, suitable cyclic deviatoric stress was applied as sinusoidal loadings at a frequency of 1 Hz under undrained conditions. This frequency ranges from 0.1 Hz to 1.5 Hz and replicates small to large earthquakes (e.g. Hussain and Sachan, 2019; Jain et al., 2021). The CSR can be written as (Table 3):

$$CSR = q_{cyc} \Big/ \left(2\sigma'_c \right) \tag{6}$$

where q_{cyc} is cyclic deviatoric stress and σ'_c is the confining stress.

Table 3 shows the information of the tests performed on both stratified and homogeneous specimens. Four different silt thicknesses (0.1H–0.4H) have been considered for interlayering with homogeneous sand. Also, after using an optimum silt thickness of 0.2H, the silt layer was placed at the top (capped soil condition), middle and bottom locations. Because of the hindrance in pore

Table 3
Static and cyclic tests.

Specimen	Silt layer thickness	Number of layers	Location of silt layer	Effective confining pressure (kPa)	Confining pressure (kPa)	Back pressure (kPa)	B	ε (%)	CSR	$D_{r,sand1}$ (%)	$D_{r,silt}$ (%)	$D_{r,sand2}$ (%)	$D_{r,m}$	e^*	$N_{cyc,L}$
NS1	0	0	N.A	100	220	120	0.99	2.96	0.26	30.2	–	30.2	30.2	0.79	3
S1	0.1H	1	M	100	220	120	0.98	2.5	0.26	29.92	70.52	30.05	40.1	0.77	4
S2	0.2H	1	M	100	200	100	0.98	2.51	0.26	30.02	71.25	29.97	47.64	0.75	6
S3	0.3H	1	M	100	240	140	0.98	2.49	0.26	31.02	70.24	29.98	53.1	0.73	5
S4	0.4H	1	M	100	240	140	0.98	2.48	0.26	30.02	72.24	30.02	57.24	0.71	3
NS2	0	0	N.A	100	260	160	0.98	2.78	0.14	30.2	–	30.20	40.1	0.77	52
S5	0.1H	1	M	100	240	140	0.98	2.51	0.14	30	71.25	30.77	40.1	0.75	57
S6	0.2H	1	M	100	220	120	0.98	2.49	0.14	29.97	72.24	29.56	47.64	0.73	187
S7	0.3H	1	M	100	220	120	0.98	2.48	0.14	29.98	70.24	30.05	53.1	0.71	79
S8	0.4H	1	M	100	240	140	0.98	2.78	0.14	30.03	70.22	29.97	57.24	0.75	48
S9	0.2H	1	T	100	200	100	0.99	2.49	0.14	–	70.02	29.98	47.64	0.75	103
S10	0.2H	1	B	100	220	120	0.98	2.48	0.14	30.05	70.23	–	46.45	0.76	225
S11	0.1H	2	MT	100	240	140	0.98	2.78	0.14	30	70	30	47.59	0.75	227
S12	0.1H	2	MB	100	200	100	0.99	2.51	0.14	30	70	30	47.63	0.75	188
S13	0.1H	2	MM	100	200	100	0.98	2.49	0.14	30	70	30	53.24	0.71	392
S14	0.1H	2	TB	100	240	140	0.98	2.48	0.14	30	70	30	47.1	0.77	245
S15	0.1H	3	TMB	100	200	100	0.99	2.78	0.14	30	70	30	47.64	0.75	560
S16	0.2H	1	M	50	190	140	0.98	2.49	0.14	29.97	71.24	29.66	47.61	0.73	Static
S17	0.2H	1	M	100	240	140	0.98	2.48	0.14	29.98	71.22	28.56	53.59	0.71	Static
S18	0.2H	1	M	150	330	180	0.98	2.96	0.14	30.02	72.54	29.62	47.63	0.75	Static
S19	0.2H	1	M	100	240	140	0.98	2.5	0.20	30.77	71.55	50.2	53.77	0.75	250
S20	0.2H	1	M	100	220	120	0.98	2.51	0.14	31.01	30.08	50.15	52.25	0.75	227
S21	0.2H	1	M	100	200	100	0.99	2.49	0.14	30.02	31.01	29.85	45.51	0.76	134
S22	0.2H	1	M	100	220	120	0.99	2.48	0.14	30	72.85	50.48	53.77	0.75	450
S23	0.2H	1	M	100	200	100	0.98	2.78	0.26	29.98	70.22	50	53.77	0.75	105
S24*	0	0	N.A.	100	240	220	0.99	2.51	0.14	30.01	–	50.74	40.52	0.79	104
S25	0.2 H	1	M	100	200	100	0.98	2.49	0.16	30.01	71.25	30.22	47.46	0.75	62
S26	0.2 H	1	M	100	200	100	0.98	2.48	0.2	30.01	70.25	30.22	47.23	0.78	29
S27	0.06H	1	T	100	220	120	0.98	2.78	0.14	30	70.24	29.96	35.76	0.78	48
S28	0.06H	1	M	100	240	220	0.99	2.49	0.14	30.02	72.24	29.66	35.81	0.78	94
S29	0.06H	1	B	100	200	100	0.98	2.48	0.14	30.05	71.25	29.86	35.87	0.78	106
NS3	H	0	Pure silt	100	220	120	0.98	2.48	0.14	–	30.25	–	30.25	0.99	35
NS4	H	0	Pure silt	100	200	100	0.98	2.96	0.2	–	30.28	–	30.28	1	9
NS5	H	0	Pure silt	100	200	100	0.98	2.96	0.26	–	30.28	–	30.28	1	2
NS6	0	0	–	100	220	120	0.98	2.50	0.14	50.02	–	50.02	50.02	0.72	98
NS7	0	0	–	100	220	120	0.98	2.51	0.16	30.24	–	30.24	30.24	0.79	38
NS8	0	0	–	100	200	100	0.99	2.49	0.16	50.25	–	50.25	50.25	0.72	72
Details of some of the additional repetitive tests															
S30=S5	0.1H	1	M	100	200	100	0.98	2.78	0.14	30	71.25	30.77	40.1	0.75	52
S31=S6	0.2 H	1	M	100	220	120	0.99	2.51	0.14	29.97	72.24	29.56	47.64	0.73	185
S32=S7	0.3 H	1	M	100	220	120	0.98	2.49	0.14	29.98	70.24	30.05	53.1	0.71	76
S33=S8	0.4 H	1	M	100	200	100	0.98	2.48	0.14	30.03	70.22	29.97	57.24	0.75	48
S34=S13	0.1 H	2	MM	100	240	140	0.98	2.78	0.14	30	70	30	57.24	0.71	390
Tests performed for the validation of developed model															
S35	0.1H	2	TB	100	240	140	0.99	2.49	0.14	30	70	30	40.1	0.77	240
S36	0.1H	3	TMB	100	220	120	0.98	2.48	0.14	30	70	30	57.64	0.75	555
S37	0.05H	1	H/4 from top	100	200	100	0.98	2.5	0.16	50.7	71.55	49.25	52.05	0.75	62
S38	0.05H	1	3H/4 from top	100	200	100	0.98	2.5	0.16	50.7	71.55	49.25	52.05	0.75	187
S39	0.2H	1	M	100	220	120	0.99	2.51	0.14	29.97	72.24	29.56	47.64	0.73	185
Strain-controlled tests performed (Strain rate, %)															
S40	0.1H	1	M	100	220	120	0.98	2.51	0.4	30	71.25	30.77	40.1	0.75	5
S41	0.1H	1	M	100	220	120	0.98	2.49	0.4	29.97	72.24	29.56	47.64	0.73	10
S42	0.1H	1	M	100	240	140	0.98	2.48	0.4	29.98	70.24	30.05	53.1	0.71	7
S43	0.1H	1	M	100	200	100	0.98	2.78	0.4	30.03	70.22	29.97	57.24	0.75	4

NS = Non-stratified, T = silt layer located at the top of the specimen, N.A.= Not applicable, M = silt layer at the middle of the specimen, B = silt layer at the bottom of the specimen, MT = silt layer at the top and middle of the specimen, MB = silt layer at the middle and bottom of the specimen, MM = silt layer at H/3 from the top and bottom of the specimen, TB = silt layer at the top and bottom of the specimen, TMB = silt layer at top, middle and bottom of the specimen, *S25 is the stratified specimen with no silt layer but with loose (upper portion) and medium dense strata (lower portion), B= Skempton's pore pressure coefficient, e^* is equivalent void ratio, $D_{r,silt}$ = relative density of the silt layer, ε = axial strain, $D_{r,sand1}$ = Relative density of the upper sand layer, $D_{r,sand2}$ = relative density of the lower sand layer.

water flow due to the less permeable silt layer, there exist both dilative and contractive zones of the sandy strata, as shown in Fig. 4. The dilative zone starts thinning due to the movement of pore-water flow from the contractive zone until it reaches dilation capacity (e.g. Kulasingam et al., 2004). The dilation capacity is the amount of water absorbed by the dilation zone of the soil mass at which the undrained shear strength diminishes to driving static shear stresses. Additionally, tests were also conducted on homogeneous sand and silt specimens to understand individual soil behavior under liquefied state.

3. Results and discussion

This section discusses the mechanism and suitability of results after cyclic triaxial tests on pure silt, pure sand and stratified specimens. In the study, specimens are considered to be liquefied instantly when the pore pressure ratio (r_u) reaches one. This theory was proposed by Seed and Lee (1966) after observing the initial liquefaction, where the effective stress becomes 0 as the pore pressure ratio (r_u) reaches unity in the isotropically consolidated specimens:

$$r_u = \frac{\Delta u}{\sigma'_{3c}} \tag{7}$$

where u is the excess pore water pressure and σ'_{3c} is the effective confining stress.

This liquefaction failure criterion has been used in the present study.

3.1. Changes in liquefaction susceptibility with an increase in silt layer thickness

Several liquefiable sites of marine or alluvial deposits contain less permeable silt layers of variable depths or patches of silty soil. Therefore, in order to replicate these geological conditions, sandy specimens were interlayered with different thicknesses of silt layer varying from 10% to 40% of the total height of the specimen. The silt thickness has been found to be a significant parameter to govern void redistribution, strain localization and related failures. Due to the overlying non-plastic silt layer, sandy strata develop a dilative zone in the upper half while 'contractive' in the lower as shown in Fig. 4. This may trigger local liquefaction failures inside the sandy zones. There exists an optimum silt layer thickness (0.2*H*, specimen S6) at which pore water migration from the contractive zone is minimum, causing an increase in $N_{cyc,L}$ to 187 when $CSR = 0.14$. But, after this thickness, due to the increased volume of non-plastic silt, specimen S8 with a silt thickness of 0.4*H* liquefies after 48 cycles. The dangerous local pore water pressure presented in the confined zone of fine sand is responsible for the overall failure of the stratified specimens. This could be justified through significant bulging around the sections of sandy strata compared to that of the silty zone (see Fig. 5). A less permeable silt layer in the sandy specimen alters the pore water pressure movement (Yamaguchi et al., 2002; Lee et al., 2014; Ecemis, 2021). This causes a hindrance in the path of water molecules around the periphery of the silt layer which results in the accumulation of localized excess pore water pressure, as shown in Fig. 4.

As a result, a significant amount of water molecules is unable to pass through silt layer and then accumulates. This is a reason behind the localized bulging at the sand-silt interface. Tasiopoulou et al. (2019) also observed a similar bulging phenomenon due to clay laminates after performing cyclic triaxial tests. Consequently,

Fig. 3. Specimen preparation and consolidation: (a) Placing and marking the latex membrane; (b) Placement of sand; (c) Placement of silt layer at the desired location; (d) Check for specimen density at the mid-stage; and (e) Image showing the location of valves and movement of water molecules during consolidation.

Table 4
Parameters used in the calculation of relative density of the stratified specimens.

Specimen	$D_{r,sand1}$ (%)	$W_{sand,1}$ (g)	$e_{sand,1}$	$R_{m,1}$	$D_{r,\ silt}$ (%)	W_{silt} (g)	e_{silt}	$R_{m,silt}$	$D_{r,sand2}$ (%)	$W_{sand,2}$ (g)	$e_{sand,2}$	$R_{m,2}$	$D_{r,\ m}$ (%)	e^*
S1	29.92	359.35	0.78	0.44	70.52	89.04	0.62	0.11	30.05	359.35	0.79	0.44	40.1	0.77
S2	30.02	319.42	0.79	0.39	71.25	178.08	0.62	0.21	29.97	319.42	0.79	0.39	47.64	0.75
S3	31.02	279.5	0.80	0.33	70.24	267.12	0.61	0.32	29.98	279.49	0.8	0.33	53.1	0.73
S4	30.02	239.6	0.79	0.28	72.24	356.16	0.61	0.42	30.02	239.57	0.79	0.28	57.24	0.71
S5	30	359.35	0.8	0.44	71.25	89.04	0.62	0.11	30.77	359.35	0.79	0.44	40.1	0.77
S6	29.97	319.42	0.79	0.39	72.24	178.08	0.62	0.21	29.56	319.42	0.79	0.39	47.64	0.75
S7	29.98	279.5	0.80	0.33	70.24	267.12	0.61	0.32	30.05	279.49	0.79	0.33	53.1	0.73
S8	30.03	239.6	0.79	0.28	70.22	356.16	0.62	0.42	29.97	239.57	0.80	0.28	57.24	0.71
S9	–	0	0.79	0	70.02	178.08	0.61	0.22	29.98	638.85	0.79	0.78	47.64	0.75
S10	30.05	718.7	0.79	0.8	70.23	178.8	0.62	0.2	–	0	–	0	46.45	0.75
S16	29.97	319.02	0.79	0.39	71.24	179.02	0.62	0.21	29.66	319.4	0.79	0.39	47.61	0.76
S17	29.98	319.1	0.79	0.39	71.22	178.02	0.62	0.2	28.56	319.1	0.79	0.38	47.59	0.75
S18	30.02	320.54	0.79	0.39	72.54	178.2	0.61	0.22	29.62	319.2	0.79	0.39	47.63	0.75
S19	30.77	320.57	0.79	0.38	71.55	179.01	0.61	0.22	50.2	330.9	0.72	0.39	53.77	0.75
S20	31.01	320.78	0.79	0.4	30.08	144.05	1	0.18	50.15	330.74	0.72	0.41	52.25	0.75
S21	30.02	320.54	0.79	0.4	31.01	144.48	1	0.18	29.85	319.78	0.79	0.4	45.51	0.76
S22	30	573.63	0.8	0.38	72.85	179.21	0.59	0.21	50.48	331.51	0.73	0.4	53.77	0.75
S23	29.98	796.51	0.79	0.38	70.22	178.08	0.62	0.21	50	330.7	0.72	0.4	53.77	0.75
S24	30.01	399.28	0.8	0.49	–	0	0.62	0	50.74	413.63	0.73	0.51	40.52	0.79
S25	30.01	319.42	0.79	0.38	71.25	178.02	0.61	0.21	30.22	330.94	0.8	0.4	47.46	0.75
S26	30.01	319.42	0.79	0.38	70.25	176.02	0.61	0.21	30.22	330.94	0.8	0.4	47.23	0.75
S27	30	176.82	0.79	0.21	70.24	50.88	0.61	0.06	29.96	596.9	0.79	0.72	35.76	0.78
S28	30.02	376.46	0.8	0.46	72.24	50.88	0.62	0.06	29.66	390	0.79	0.47	35.81	0.78
S29	30.05	576.1	0.79	0.71	71.25	50.88	0.62	0.06	29.86	183.17	0.79	0.22	35.87	0.78

Note: $W_{sand,1}$ = Weight of the upper sand layer, $R_{m,1}$ = percentage of the dry weight of the upper sand layer in the stratified soil strata, W_{silt} = Weight of the silt layer, $R_{m,silt}$ = percentage of the dry weight of the silt layer in the stratified soils, $W_{sand,2}$ = Weight of the lower sand layer, $R_{m,2}$ = percentage of the dry weight of the lower sand layer in the stratified soils, $e_{sand,1}$ = void ratio of the upper sand layer, e_{silt} = void ratio of the silt layer, $e_{sand,2}$ = void ratio of the lower sand layer.

the vulnerable strata located at the lower or upper side of the silt layer may liquefy depending on the initial states and loading conditions. The severity of failure could be understood by the development of wider cracks (2–3 cm) in specimens S7 and S8, as shown in Fig. 6, due to the higher instability of specimens with larger silt thickness. Similar observations were noticed by Jia and Bingye (2012) and Xiu et al. (2019), where after an optimum silt thickness, the resistance against liquefaction receded. A homogeneous specimen of silt (NS3) liquefied in merely 35 cycles, which was due to the absence of plastic minerals responsible for binding between soil particles. Meanwhile, due to the internal friction between sub-rounded sand particles, homogeneous sand specimens liquefied in 68 cycles.

The variation of excess pore water pressure vs. number of cycles is presented in Fig. 7. At four different silt thicknesses, pore flow movement varies according to the hindrance developed. It can be noticed that the development rate of excess pore water pressure was highest in specimen S8 and least in specimen S6 with optimum silt thickness. In Fig. 7a, it can be seen that in the first cycle of loading, there exists very small amount of negative excess pore water pressure. The mechanism behind this observation is the generation of dilation type characteristics just after the application of loading. The particles of sand-silt readjust themselves creating a tension in the water molecules which are ultimately responsible for the development of negative excess pore water pressure (Fig. 7b).

3.2. Effect of CSR on the liquefaction susceptibility

The response of soil specimens at a higher CSR value will help in predicting the liquefaction failures under increased seismic disturbances. After increasing a *CSR* value from 0.14 to 0.26, the concept of optimum silt thickness was less valuable. The pore pressure development was too quick due to increased deviatoric stresses, as shown in Fig. 8a. Therefore, all the specimens (S1, S2 and S3) liquefied within 12 cycles at $CSR = 0.26$. Therefore, the pore pressure generation rate is nearly the same for all stratified cases reflecting the low impact of silt thickness variation on excess pore water pressure rate at higher deviatoric stresses. To replicate the influence of increment in earthquake vibrations or loading rate, four different CSRs (Specimens S2, S6, S25 and S26) were chosen at a silt thickness of 0.2*H* or 28 mm as shown in Table 3. It can be seen in Fig. 8b that the number of failure cycles rises to 37 times when the *CSR* value decreased from 0.26 to 0.14. At higher deviatoric stresses, a more considerable amount of pore-water flow is expelled from the developed contractive zone to the dilative zone at all the silt thicknesses. To closely assess the development rate of pore pressure, Fig. 8c presents the changes in maximum pore pressure ratio with $N_{cyc,L}$ required to attain liquefaction in the specimens with a silt thickness of 0.2*H* (28 mm). The development rate of pore pressure was too quick in specimens S2 and S26 while it was gradual for specimens S6 and S25.

Fig. 9 consists of three stress-paths for specimens at $CSR = 0.26$. Even so, the number of failure cycles is nearly the same but the trend of $q - p'$ is different. The reason behind this phenomenon was the similar development rate of pore water pressure at all silt layer thicknesses. In Fig. 9, it can be observed that as the cyclic loading touches the phase transformation line (PTL), the instability develops in the specimen. In the end, the failure of the specimen occurs when cyclic loading reaches failure line (FL). Xu et al. (2020) observed a 'continued liquefaction' stage at which the effective stress of the sandy specimen appeared to be negligible in cyclic triaxial tests. Both PTL and FL have been drawn using the static tests performed on the stratified specimen at three different confining stresses (e.g. Vaid et al., 2001).

3.3. Significance of silt layer locations

Silt layer may exist even at several depths in the actual field; therefore, to replicate such a field situation, silt was placed at three different locations, i.e. the top (capped soil condition), middle and bottom of the specimen. The optimum silt layer thickness (0.2*H*) has been chosen for this observation. Xiu et al. (2019) also observed that when the depth of the silt layer increased from top to bottom, the value of $N_{cyc,L}$ also increased. It has been found that the

Table 5
Time required for the consolidation of the specimens.

Test specimen code	Silt layer thickness	No. of layers	Location of silt layer	Effective confining pressure (kPa)	Confining pressure (kPa)	Back pressure (kPa)	B	t_{conso} (min)	$D_{r,m}$	e^*
NS1	0	0	N.A	100	220	120	0.99	25	30.2	0.79
S1	0.1H	1	M	100	220	120	0.98	38	40.1	0.77
S2	0.2H	1	M	100	200	100	0.98	42	47.64	0.75
S3	0.3H	1	M	100	240	140	0.98	48	53.1	0.73
S4	0.4H	1	M	100	240	140	0.98	58	57.24	0.71
NS2	0	0	N.A	100	260	160	0.98	24	40.1	0.77
S5	0.1H	1	M	100	240	140	0.98	28	40.1	0.75
S6	0.2H	1	M	100	220	120	0.98	41	47.64	0.73
S7	0.3H	1	M	100	220	120	0.98	48	53.1	0.71
S8	0.4H	1	M	100	240	140	0.98	60	57.24	0.75
S9	0.2H	1	T	100	200	100	0.99	37	47.64	0.75
S10	0.2H	1	B	100	220	120	0.98	45	46.45	0.76
S11	0.1H	2	MT	100	240	140	0.98	62	47.59	0.75
S12	0.1H	2	MB	100	200	100	0.99	65	47.63	0.75
S13	0.1H	2	MM	100	200	100	0.98	66	53.24	0.71
S14	0.1H	2	TB	100	240	140	0.98	66	47.1	0.77
S15	0.1H	3	TMB	100	200	100	0.99	78	47.64	0.75
S16	0.2H	1	M	50	190	140	0.98	42	47.61	0.73
S17	0.2H	1	M	100	240	140	0.98	41	53.59	0.71
S18	0.2H	1	M	150	330	180	0.98	43	47.63	0.75
S19	0.2H	1	M	100	240	140	0.98	41	53.77	0.75
S20	0.2H	1	M	100	220	120	0.98	42	52.25	0.75
S21	0.2H	1	M	100	200	100	0.99	41	45.51	0.76
S22	0.2H	1	M	100	220	120	0.99	43	53.77	0.75
S23	0.2H	1	M	100	200	100	0.98	41	53.77	0.75
S24*	0	0	N.A.	100	240	220	0.99	25	40.52	0.79
S25	0.2H	1	M	100	200	100	0.98	41	47.46	0.75
S26	0.2H	1	M	100	200	100	0.98	42	47.23	0.78
S27	0.06H	1	T	100	220	120	0.98	35	35.76	0.78
S28	0.06H	1	M	100	240	220	0.99	33	35.81	0.78
S29	0.06H	1	B	100	200	100	0.98	32	35.87	0.78
NS3	H	0	Pure silt	100	220	120	0.98	90	30.25	0.99
NS4	H	0	Pure silt	100	200	100	0.98	92	30.28	1
NS5	H	0	Pure silt	100	200	100	0.98	93	30.28	1
NS6	0	0	–	100	220	120	0.98	26	50.02	0.72
NS7	0	0	–	100	220	120	0.98	27	30.24	0.79
NS8	0	0	–	100	200	100	0.99	25	50.25	0.72
S30=S5	0.1H	1	M	100	200	100	0.98	37	40.1	0.75
S31=S6	0.2H	1	M	100	220	120	0.99	42	47.64	0.73
S32=S7	0.3H	1	M	100	220	120	0.98	48	53.1	0.71
S33=S8	0.4H	1	M	100	200	100	0.98	59	57.24	0.75
S34=S13	0.1H	2	MM	100	240	140	0.98	64	57.24	0.71
S35	0.1H	2	TB	100	240	140	0.99	68	40.1	0.77
S36	0.1H	3	TMB	100	220	120	0.98	80	57.64	0.75
S37	0.05H	1	H/4 from top	100	200	100	0.98	40	52.05	0.75
S38	0.05H	1	3H/4 from top	100	200	100	0.98	44	52.05	0.75
S39	0.2H	1	M	100	220	120	0.99	41	47.64	0.73

t_{conso} = time required from consolidation;*S24 is the stratified specimen with no silt layer but with loose (upper portion) and medium dense strata (lower portion).

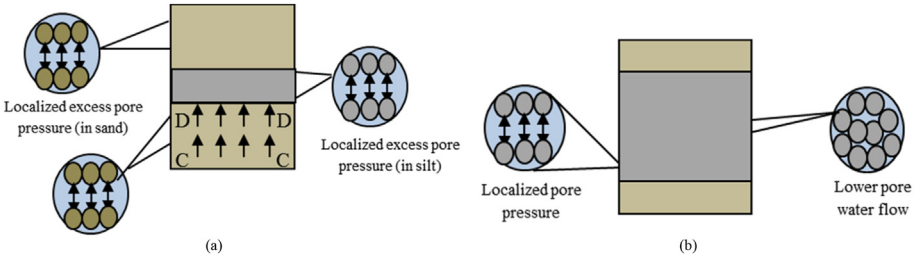

Fig. 4. Specimen with silt layer with different thicknesses: (a) 0.1H and (b) 0.4H (D = dilative zone, C = compressive zone).

placement depth (location) of the silt layer has a vital role in controlling the quantity of pore-water flow across the underlying liquefiable sand. The development rate of excess pore water pressure was highest in the case of capped soil conditions compared to the other silt locations (Fig. 10). The increment rate of pore pressure was very high when the silt layer was located at the top (Fig. 10). Under these circumstances, a larger volume of pore water migrates towards the loose dilative zone from the contractive zone, as shown in Fig. 11a. Consequently, a rise in void ratio or loosening of the dilative zone is attributed to strain localization. Meanwhile, after

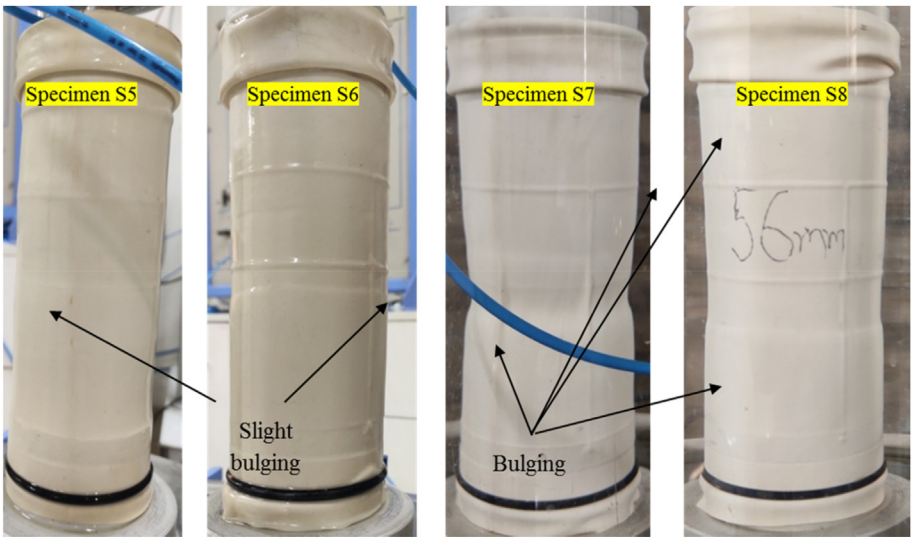

Fig. 5. Specimen showing bulging phenomenon in the specimen with silt layer at a thickness of (a) 0.1*H*; (b) 0.2*H*; (c) 0.3*H* and (d) 0.4*H*.

increasing depth of the silt layer from the top of the specimen, the water expelled from the contractive zone is reduced and ultimately a reduction in the potential loosening of underlying soil mass is observed (Fig. 11b and c). Therefore, more cycles are required to liquefy the specimen when the silt layer is placed at larger depths, as shown in Table 3.

When the silt layer was located at the bottom of the specimen (S10), overlying sandy soil existed only in the contractive phase with no strain localization. Here, the silt layer provided additional strength to the whole specimen, thereby decreasing the liquefaction susceptibility which resulted in 225 cycles to liquefy the specimen. Tasiopoulou et al. (2019) replicated the geology of soil strata closer to the alluvial deposits, marine strata and intertidal sites containing clay laminates, where the role of stratification was investigated numerically and experimentally. Significant bulging was observed in soil mass with laminated deposits using both cyclic triaxial tests and numerical simulations. A similar observation was noted in the present work using cyclic triaxial. In such cases, the hindrance developed by less permeable silt layer modifies pore water flow movement. This is a reason for the localized bulging at significant locations i.e. nearer to the top, middle and bottom, as shown in Fig. 12. Significant cracks are visible in specimen S9, leading to the early failure of the whole specimen (Fig. 13). Meanwhile, specimen S10 was intact without any crack, depicting higher stability than others. In the investigation conducted by Tasiopoulou et al. (2019), it was observed that the clay laminations enhanced the liquefaction resistance of the specimen tested. The plasticity index of these clay laminates was 20%–45%, and the liquid limit was greater than 50%. These clay laminates receded the pore pressure development due to plasticity characteristics and minimized the liquefaction susceptibility. This is the main reason behind the termination of localized liquefaction or void-redistribution. It could

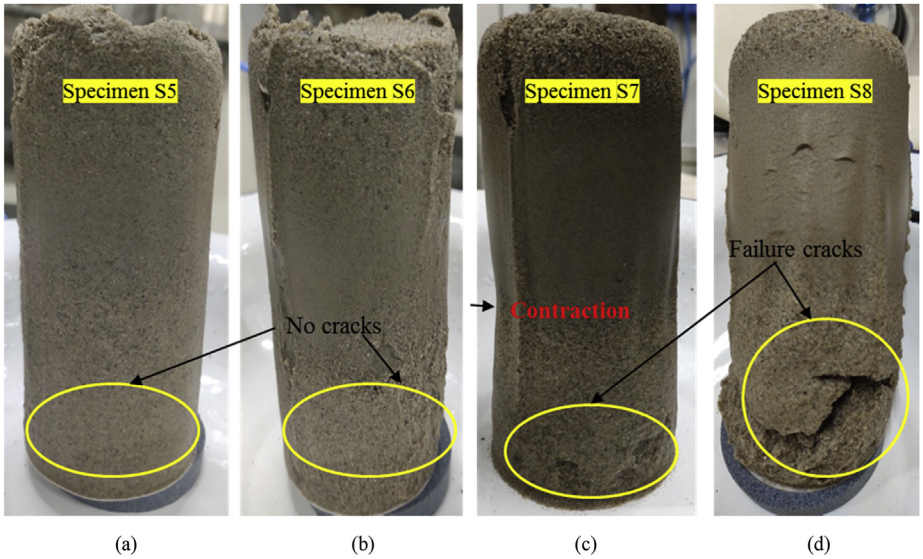

Fig. 6. Cracks developed where silt layer was used at a thickness of (a) 0.1*H*, (b) 0.2*H*, (c) 0.3*H*, and (d) 0.4*H*.

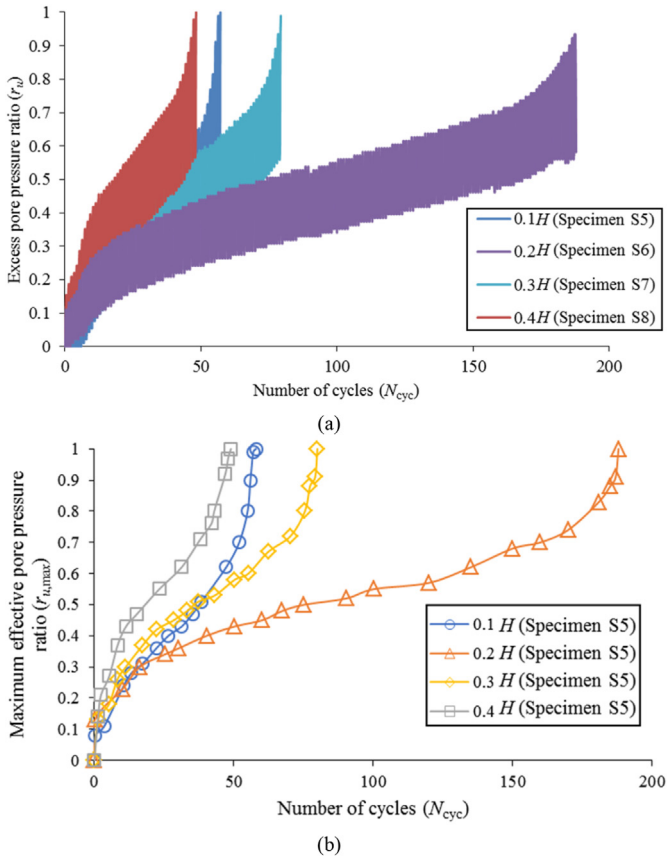

Fig. 7. Specimen interlayered with different silt thicknesses: (a) Excess pore pressure ratio vs. number of cycles; and (b) Maximum effective pore pressure ratio vs number of cycles.

be understood using several criteria for liquefaction susceptibility, where the content and plasticity characteristics of fine content play a vital role (Andrews and Martin, 2000). In the study, a non-plastic silt layer was used as an interlayer to prepare the stratified samples. The permeability of the used silt was less than 1/100 times that of the fine sand. Therefore, the governing parameters for the liquefaction of stratified specimens are the differences in permeability of sand and silt rather than the plasticity characteristics of the silt layer.

3.4. Effect of different silt layers on liquefaction phenomenon

This section considers more than one layer of less permeable silty soil to replicate natural stratification, where a silt thickness of 0.1H was used (rather than 0.2H) due to experimental limitations. Fig. 14 shows three cross-sections of specimens S11 and S14 with two silt layers whereas S15 has three silt layers. As discussed in the earlier sections, each sand layer develops vulnerable localized excess pore water pressure in the fine sand layer causing bulging of the specimen and resulting in liquefaction failure, as shown in Fig. 15. Due to the restricted movement of pore-water flow near the silt layer, a localized bulging can be observed at the interface of sand-silt. With an increased number of silt layers, the total volume of pore water expelled through the contractive to the dilative zone is also reduced to a safety limit. Therefore, bulging limits itself at a certain level without significantly affecting the specimen.

The localized failure of sand sub-layers is caused by the generation of higher pore pressure under cyclic loadings, which causes redistribution of the voids and strain localization. Due to the clay laminations, this effect was significantly reduced, causing an increment in liquefaction resistance (Tasiopoulou et al., 2019). Similarly, with an increase in the number of silt layers, the liquefaction resistance of the overall specimen also increases. It can be observed in Fig. 16a and b that the insertion of more silt layers (two or three) is responsible for developing several dilative and contractive zones. As shown in Fig. 17, the number of silt layers increases from single to triple where $N_{cyc,L}$ value reaches more than the 500 mark (Table 3). More silt sub-layers divide the specimen into a greater number of soil sections, which is a reason for the reduction in excess pore water pressure (Fig. 17). Here, it can be observed that a consistent loading pattern can also liquefy a stable

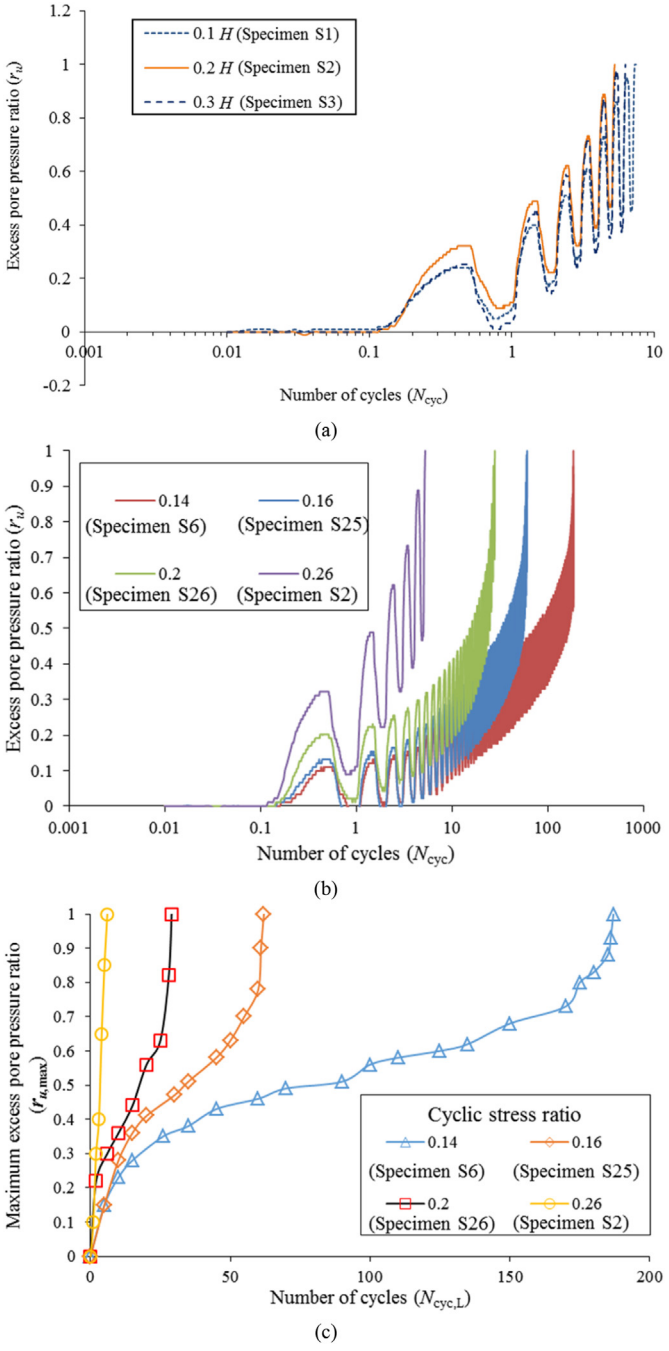

Fig. 8. (a) Excess pore pressure ratio versus N_{cyc} at $CSR = 0.26$; (b) Excess pore pressure ratio versus N_{cyc} at different CSR; and (c) Maximum excess pore pressure ratio versus $N_{cy,L}$ at different CSR.

stratified specimen after a sufficiently long duration of cyclic loadings. This shows that the generation of pore pressure was slow and steady but it was disastrous for the long-duration earthquakes which could be neglected in most liquefaction-related studies. Therefore, such an observation is quite important.

3.5. Influence of relative firmness of soil layers on the liquefaction susceptibility of the stratified specimen

The soil stratification nearby several marine or alluvial sites possesses a combination of sand-silt layers at variable densities. In sections 3.3 and 3.4, the influence of silt thickness and silt layer location was responsible for governing the liquefaction susceptibility of the overall specimen. Several researchers have noticed the crucial role of soil density on the liquefaction using cyclic triaxial tests (e.g. Tasiopoulou et al., 2019; Monkul et al., 2021; Zhang et al., 2021). However, the relative firmness of stratified soil layers also governs the vulnerability of the soil strata against liquefaction initiation. Fig. 18a shows the variation of r_u for the specimens S24, S21, S6 and S22 (Table 3). In all of the specimens, S24 was most vulnerable due to the absence of resistance provided in presence of the silt layer. There was about a 79% increase in $N_{cyc,L}$ value in specimen S6 compared with S24. The reason is the increment in the densities of the silt layer and sand layer (located beneath the silt layer). Due to the increment in particle-particle interaction at higher density, the rate to pore pressure generation is also receded (Fig. 18). In can be seen that the rate of r_u increases order-wise in the specimens S24, S21, S6 and S22, due to the enhancement in firmness of the silt layer and sandy strata. There exists a unique density (modified density) of the overall stratified specimen, as shown in Table 4, which is calculated as suggested by Yoshimine and Koike (2005). Additionally, the relative firmness or density of soil layers was responsible for deformation and shrinking of specimen diameter. It can be seen in Fig. 18b that there exists a demarcation surface between the interfaces of silt-sand strata. The demarcation surfaces C1 and C2 are clearly visible on the liquefied specimens S21 and S6 with a diameter reduction of about 2 cm. Also, when the relative density of the lower sandy strata increases, the demarcation surface (C3) is rarely visible. This is due to the decrement in pore water migration and resistance developed by the silt layer.

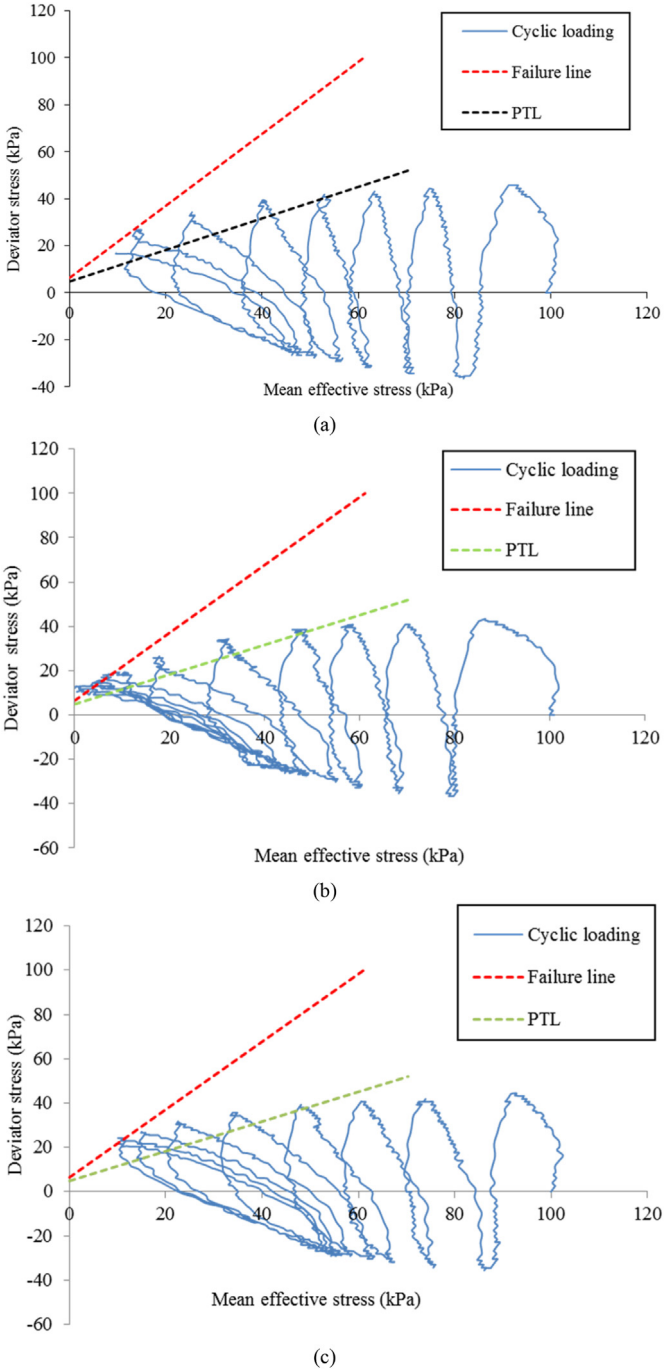

Fig. 9. Stress-path for the specimens (a) S1; (b) S2 and (c) S3.

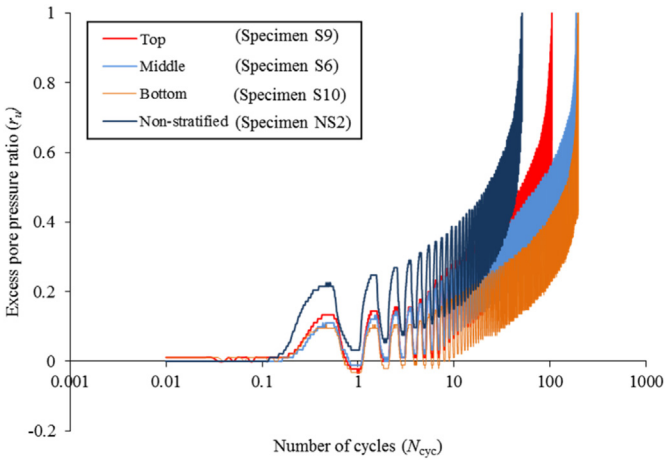

Fig. 10. Excess pore pressure ratio versus number of cycles of the specimen interlayered with silt at top, middle and bottom of the specimen.

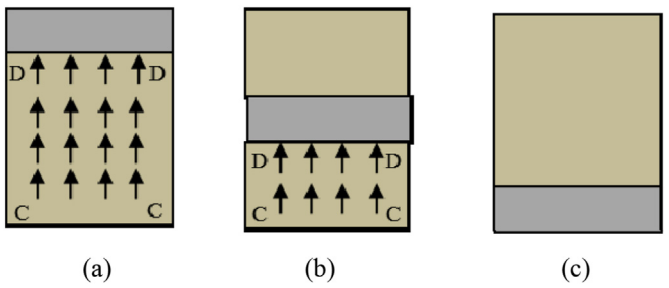

Fig. 11. Mechanism of pore water flow at different silt layer locations: (a) Top, (b) Middle, and (c) Bottom.

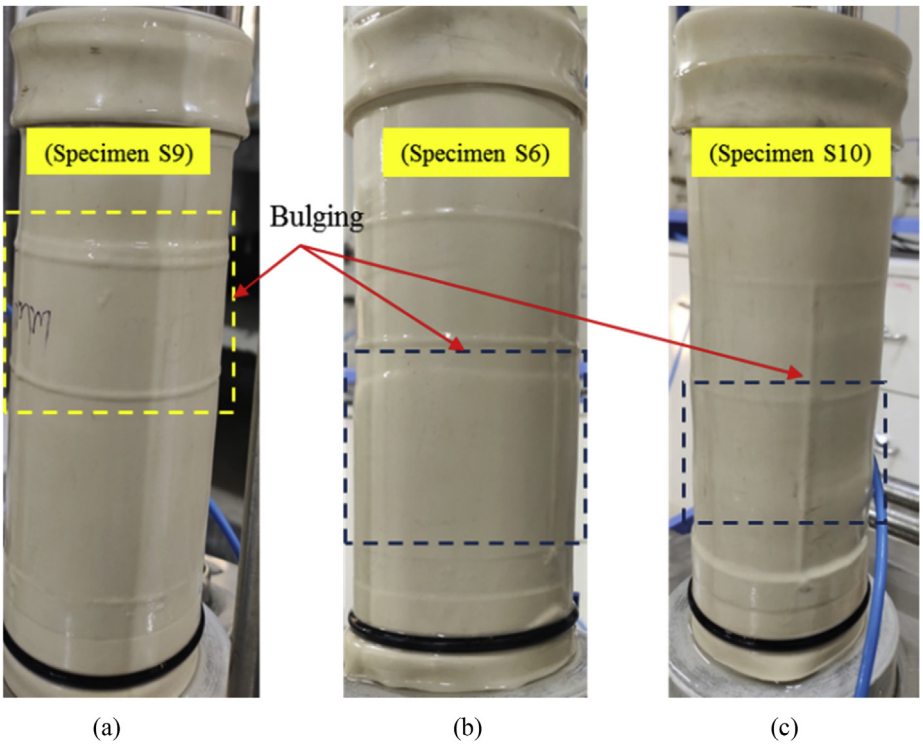

Fig. 12. Bulging of the specimens when the silt layer located at (a) Top, (b) Middle, and (c) Bottom.

3.6. Comparison with previous works

The comparison of the present work with the previous studies (Tasiopoulou et al., 2019; Xiu et al., 2019) is presented in this section. A comparison of the present work with the findings of Xiu et al. (2019) is presented in Fig. 19a and b, which show the variation of $N_{cyc,L}$ vs. silt thickness and $N_{cyc,L}$ vs. locations of silt layer. Xiu et al. (2019) conducted strain-controlled cyclic triaxial tests at effective confining pressure of 50 kPa, but a similar nonlinear relation of $N_{cyc,L}$ has been established with silt thickness in this study at a confining pressure of 100 kPa. Authors found the optimum silt layer thickness (t_{opt}) as $0.3H$ at which liquefaction susceptibility was minimum, but in the present study t_{opt} was obtained as $0.2H$ at $CSR = 0.14$ (Fig. 19a). The concept of t_{opt} was found to be less useful as described in Section 3.1 at $CSR = 0.26$. With an increment in deviatoric stresses to 40 kPa or 50 kPa, a large amount of pore pressure is generated in the whole specimen which causes localized liquefaction in different zones of the stratified specimen.

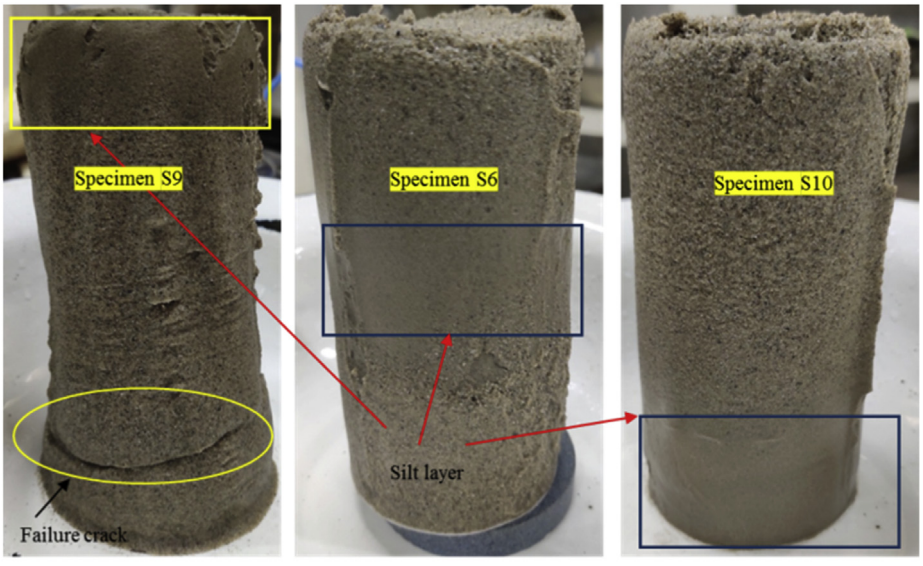

Fig. 13. Failure cracks in the specimens when the silt layer located at (a) Top; (b) Middle and (c) Bottom.

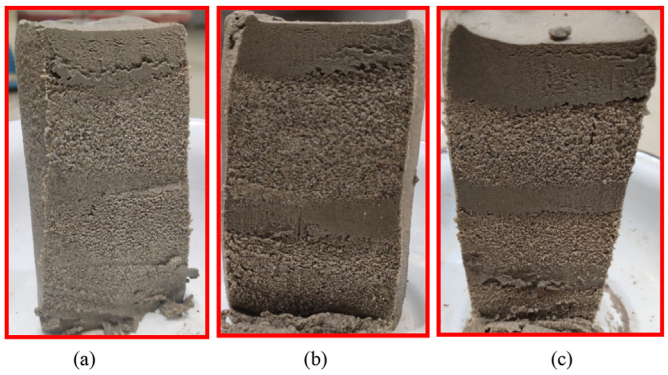

Fig. 14. Cross-section of the specimens (a) S14; (b) S11 and (c) S15.

In such cases, the resistance provided by the silt layer was limited, therefore there was a marginal difference in $N_{cyc,L}$ values for the specimens (S1 to S4) at higher *CSR* values. Fig. 19b shows the impact of silt layer location (z) on $N_{cyc,L}$. Due to low confining stresses, $N_{cyc,L}$ seems to be lower in the study of Xiu et al. (2019), but this trend is similar to that in the present study, i.e. as the value of '*d*' increases, $N_{cyc,L}$ also increases. The liquefaction resistance curve in the present research has been plotted with the findings of Tasiopoulou et al. (2019) (see Fig. 19c). This can be easily understood by the trend line of the present study, which follows a similar pattern as suggested by Tasiopoulou et al. (2019). Meanwhile, more than 200 cycles were required to attain liquefaction when multiple silt layers were used, as shown in Fig. 19c.

Due to the resistance provided by the silt layer, the number of cycles to attain liquefaction was higher for the stratified specimens. Therefore, the plot of the stratified specimen lies above the pure sand specimens. Additionally, the curve of pure silt specimens lies below all the plots because of the lower liquefaction resistance. Similar results were also obtained by Singh (1996) where the liquefaction resistant curve of the homogeneous silt specimens was located below the curves of pure sand specimens. It was due to the sudden rise in the rate of excess pore water pressure inside the silty material.

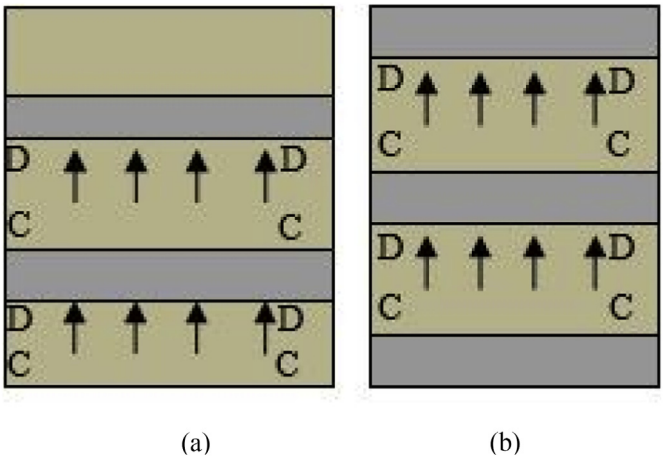

Fig. 16. Mechanism of pore water flow with different silt layers: (a) Two silt layers and (b) Three silt layers.

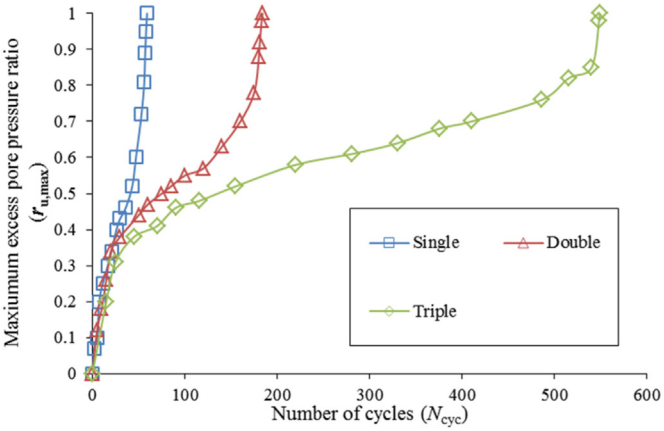

Fig. 17. Maximum excess pore pressure ratio vs. number of cycles for the specimens interlayered with single, double and triple silt layers.

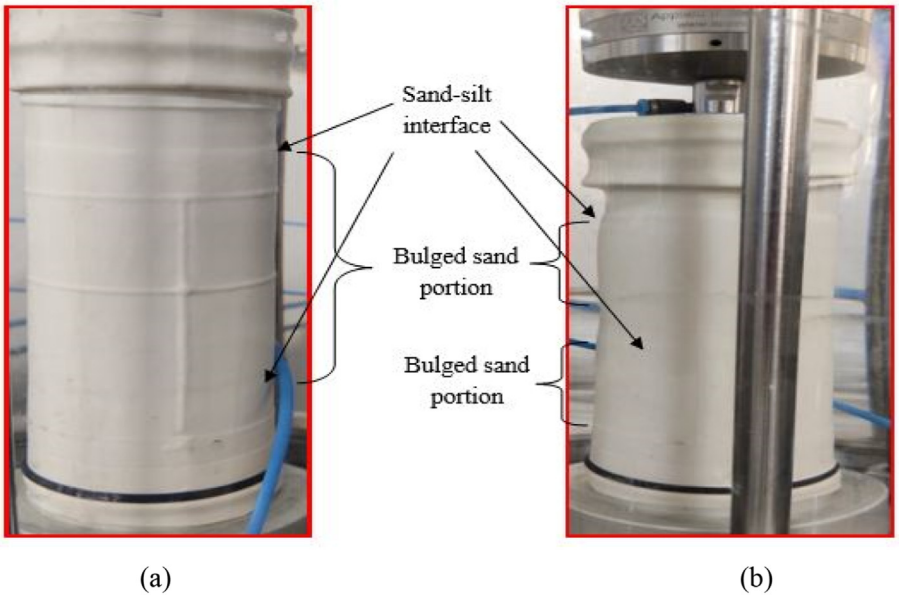

Fig. 15. Bulged sand portions in the specimens (a) S11 and (b) S14.

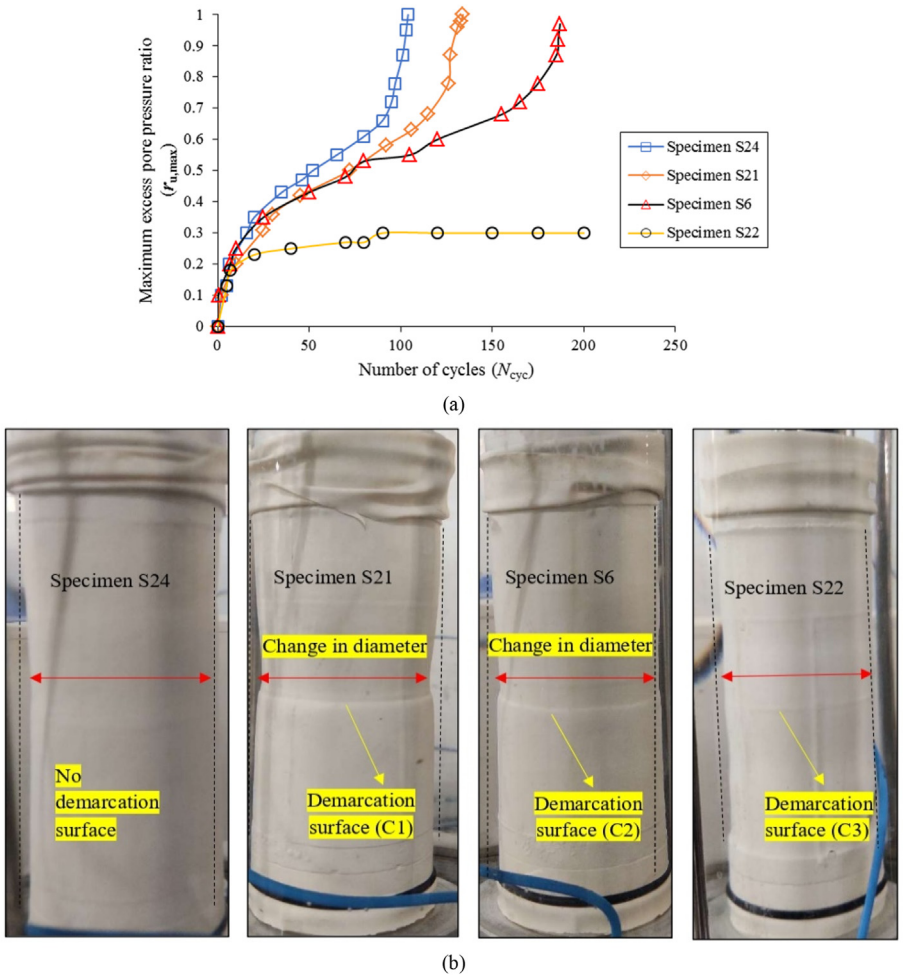

Fig. 18. Specimen at different modified densities: (a) Variation of maximum excess pore pressure ratio versus number of cycles; and (b) Images of liquefied specimen with changes in diameter.

3.7. Regression analysis

3.7.1. Development of regression model

Using the results obtained, multiple nonlinear regression analysis was performed and models have been proposed for calculation of the failure cycles to cause liquefaction ($N_{cyc,L}$) using IBM SPSS Statistics 27.0.1 software. A generalized model is developed using significant parameters, i.e. deviatoric stresses, thickness, location, density and number of silt layers used in the stratified soil specimens.

In all the stratified specimens, the silt layer governed liquefaction resistance, which ultimately affected $N_{cyc,L}$. Firstly, a strong correlation of $F(CSR)$, $F(n)$, $F(D_{r,m})$ $F(t)$ and $F(z)$ was checked with $N_{cyc,L}$, as shown in Fig. 20a–e. $F(t)$, $F(z)$, $F(n)$ are the functions of thickness, location and number of silt layers. Further, using all the significant parameters, a multi-linear regression model has been developed after utilizing normalized relations i.e. t/H and z/H, for a better applicability.

Using constant depth (location) and thickness of silt layer, Fig. 20a is plotted using different CSR values. Here, $R^2 = 0.981$ suggests a satisfactory relationship between $N_{cyc,L}$ and CSR. Fig. 20b depicts the trend line of $N_{cyc,L}$ with the number of silt layers used in stratified specimens at $CSR = 0.14$. Here, $R^2 = 0.997$ indicates the correct usage of power relationship. The relative firmness of the sand-silt combination has a significant effect on liquefaction susceptibility. This could be understood through Fig. 20c, where a strong correlation between $N_{cyc,L}$ and $D_{r,m}$ is presented with $R^2 = 0.98$. Fig. 20d shows the effect of different silt thicknesses (t) on $N_{cyc,L}$ at $CSR = 0.14$ and with a single silt layer at $H/2$ from the top. The regression analysis was performed in two different parts because of the behavior of trend line between number of failure cycles ($N_{cyc,L}$) and silt layer thickness (t). It can be observed that this trend line shows opposite pattern on the two sides of optimum silt thickness (t_{opt}) and consists of following two parts: (i) Rising limb: $N_{cyc,L}$ vs. $0 \leq t \leq 0.2H$, and (ii) Falling limb: $N_{cyc,L}$ vs. $0.2H \leq t \leq H$.

In Fig. 20d, it can be seen that the value of R^2 above 0.95 for the two different sides of limbs is quite satisfactory. Therefore, there exists a strong 'power' relationship. Apart from single silt layer, this model has been developed after interlayering two or three silt layers also, where it is not justified to utilize normal silt layer thickness (t) or normal silt layer location (z). Therefore, equivalent thickness (t^*) and equivalent location (z^*) have been calculated using Eqs. (8) and (9), which were helpful in the calculation of $N_{cyc,L}$ using the proposed model:

$$t^* = \sum_{i=1}^{i=n} t_i z_i \Big/ \sum_{i=1}^{i=n} z_i \tag{8}$$

$$z^* = \sum_{i=1}^{i=n} t_i z_i \Big/ \sum_{i=1}^{i=n} t_i \tag{9}$$

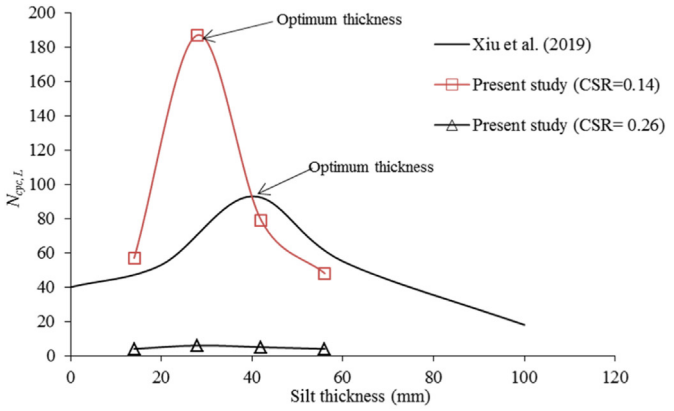

(a)

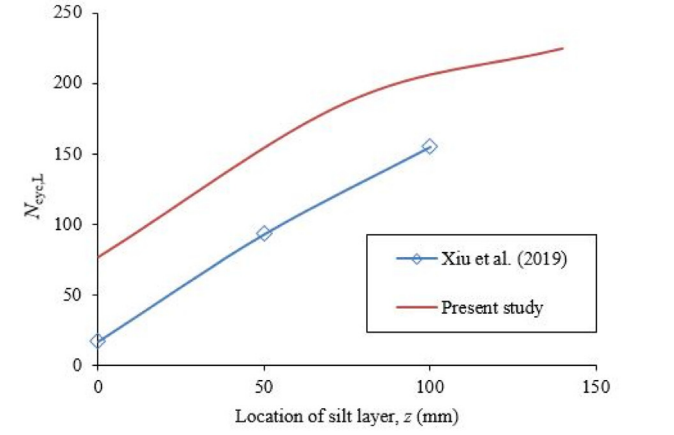

(b)

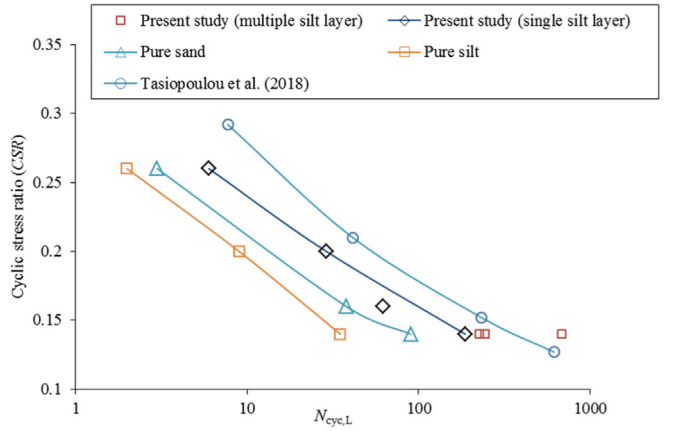

(c)

Fig. 19. Comparison with previous studies: (a) Comparison for silt layer thicknesses; (b) Comparison for the location of silt layer; and (c) Liquefaction-resistant curves.

where t_i is the thickness of ith silt layer, and z_i is the location of ith silt layer from top of the specimen.

To observe the effect of silt placement location on $N_{cyc,L}$, Fig. 20e is presented for a constant thickness (28 mm) and deviatoric stress (28 kPa) with different silt locations. The power relation with $R^2 = 0.986$ depicts the strong relation between (z/H) and $N_{cyc,L}$.

After utilizing all of the above relationships between $N_{cyc,L}$, σ_d/σ'_c, t/H and d/H, regression model is presented for the stratified specimens as

$$N_{cyc,L} = a\left(\frac{\sigma_d}{2\sigma'_c}\right)^b n^c (D_{r,m})^d \left(1+\frac{t}{H}\right)^e \left(1+\frac{d}{H}\right)^f \quad (10)$$

where a, b, c, d, e and f are regression coefficients in Table 6, and σ_d is deviatoric stress.

Eq. (10) is divided into two sections on the basis of optimum thickness obtained at 28 mm (i.e. 0.2H) in this study (Table 6). The coefficients c, d and f are responsible for increasing the value of $N_{cyc,L}$, therefore, they are positive for both sections. The value of coefficient 'e' is positive below 0.2H but negative afterward which depicts the presence of optimum thickness. Also, $\sigma_d/2\sigma'_c$ or CSR supported a decreasing trend, this is why 'b' is negative for both the sections.

3.7.2. Validity of the regression models

To check the adequacy of the proposed model, a comparative analysis has been performed. The number of cycles required to attain liquefaction ($N_{cyc,L}$) obtained by Xiu et al. (2019) was based on strain-controlled tests; therefore, its deviatoric stresses at liquefaction failure were considered for calculation of the CSR. Xiu et al. (2019) considered an effective confining pressure of 50 kPa and with a specimen diameter of 50 mm. Apart of those differences, the developed model is predicting satisfactory values of number of failure cycles to reach liquefaction. Fig. 21 shows the validation of the proposed model with the validatory tests on specimens S30, S31, S34 and S36 (Table 3), where a strong correlation can be observed with $R^2 = 0.95$. This ensures the efficacy of the proposed model in both the loose and medium dense conditions.

3.8. Micro-characterization of the stratified specimen using SEM analysis

This section deals with the micro-characterization of soil specimens. This analysis facilitated an understanding of the resistance provided by the silt layer and the venting out phenomenon. A sufficient amount of sand or silt content on the analyzed section indicated the breaking of the silt seam and its dissipation. A comparison has been made for the effect of silt thicknesses (0–0.4H) and the effect of location where the silty material has a vital role in assessing the failure mechanism.

3.8.1. Role of silt layer thickness in micro characterization

A critical investigation of soil stratification has been performed using micro-characterization through SEM images. In Section 3.1, it has been understood that the resistance provided by the optimum silt thickness (0.2 H or 28 mm) was found to be the highest. Similarly, it can be seen in Fig. 22c and d that the silt content is minimal because a very small amount of silty material is transported in the upper sections for specimen S5. While in specimen S8, with a silt thickness of 56 mm, instability was triggered due to a limited hindrance provided by the silt layer. This causes the traveling of silt particles into the upper regions of the specimen under the action of dissipated pressures (see red circle in Fig. 22g and h). On the other hand, specimens S5 and S7 provided a limited resistance; therefore a scattered framework of sand-silt can be seen in Fig. 22a, b, e, and f. The developed regression model (Eq. (10)) also indicated a similar phenomenon, where the resistance towards liquefaction was found to be the highest for the specimen with an optimum silt thickness.

3.8.2. Role of silt layer location in micro characterization

The impact of silt layer location on the liquefaction susceptibility of the stratified specimen has been investigated (e.g. Xiu et al., 2019; Jain et al., 2022). The vulnerability towards liquefaction increases as the placement depth of the silt layer increases. A similar

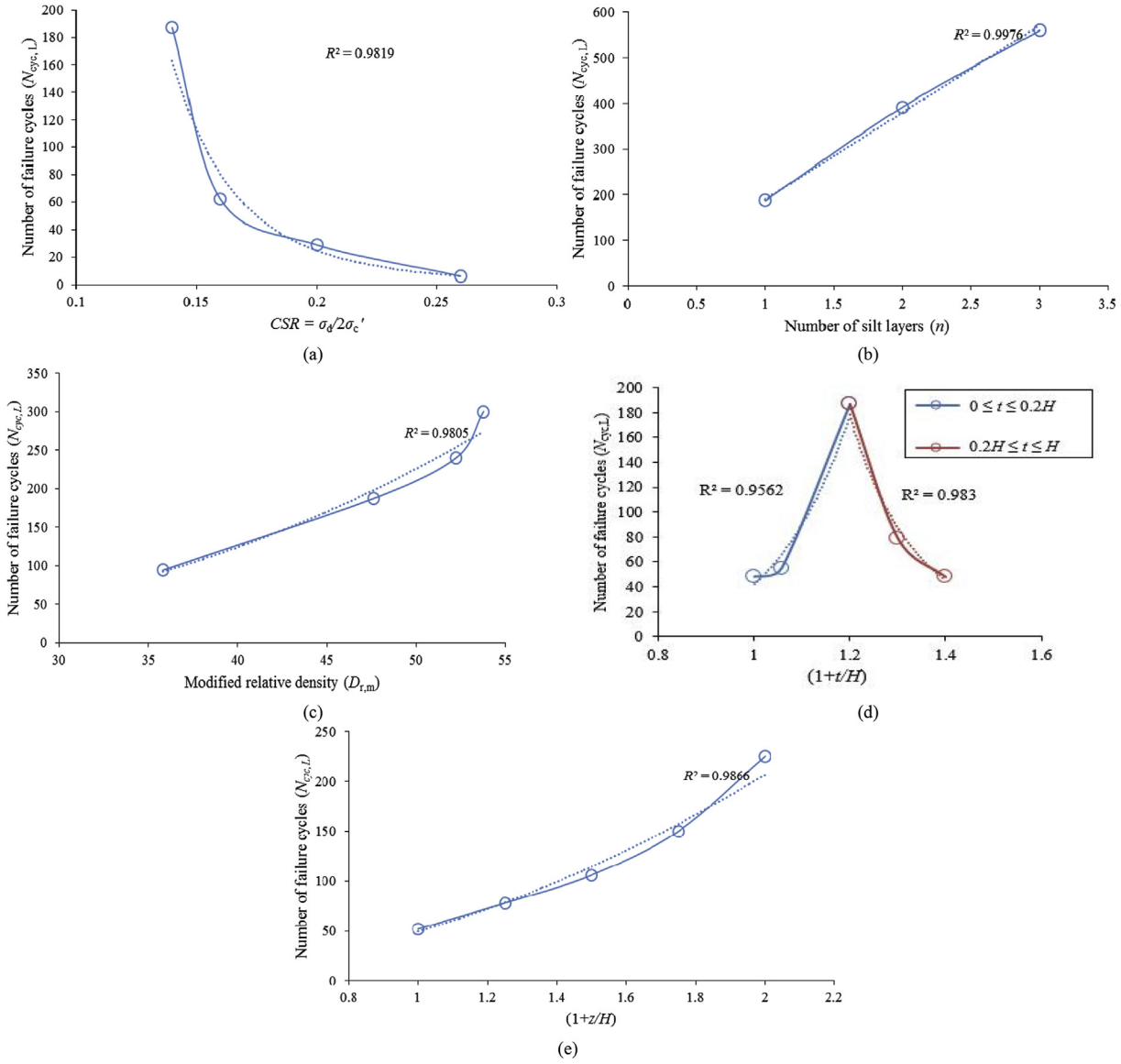

Fig. 20. Correlation of all the significant parameters with number of cycles required to attain liquefaction ($N_{cyc,L}$): (a) CSR with $N_{cyc,L}$; (b) Number of silt layers (n) used with $N_{cyc,L}$; (c) Modified relative density ($D_{r,m}$) with $N_{cyc,L}$; (d) Silt thickness (t) with $N_{cyc,L}$; and (e) Silt locations (z) with $N_{cyc,L}$.

statement can be made using the micro-characterization analysis of the specimen with an optimum silt thickness of 0.2 H or 28 mm. When the silt layer was situated on the top of the specimen (S9), the sand particles located below vented out after breaking the silt layer. This was due to the sudden dissipation of excess pore water. This could be justified using Fig. 23a where the uniform distribution of sand-silt is clearly visible. Additionally, when the silt layer was at the bottom of the specimen (Fig. 23c), nearly no-silt particle traveled to the top, which may be due to a sufficient resistance against liquefaction triggering. At the middle position of silt layer (specimen S6), scattered distribution of sand-silt can be seen in the SEM image (Fig. 23b). This analogy also aligns in line with the

Table 6
Regression coefficients of the proposed model.

t value	a	b	c	d	e	f
[0, 0.2H]	1.28×10^{-11}	−7.164	1.052	3.23	8.45	1.001
[0.2H, H]	1.10×10^{-8}	−5.944	1.007	3.28	−8.1	1.352

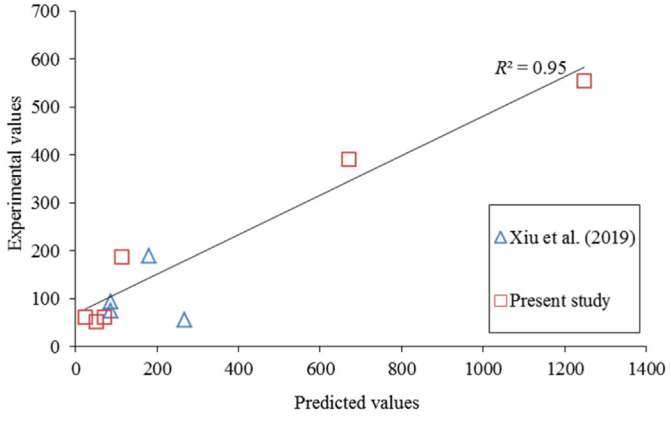

Fig. 21. Validation of the proposed model.

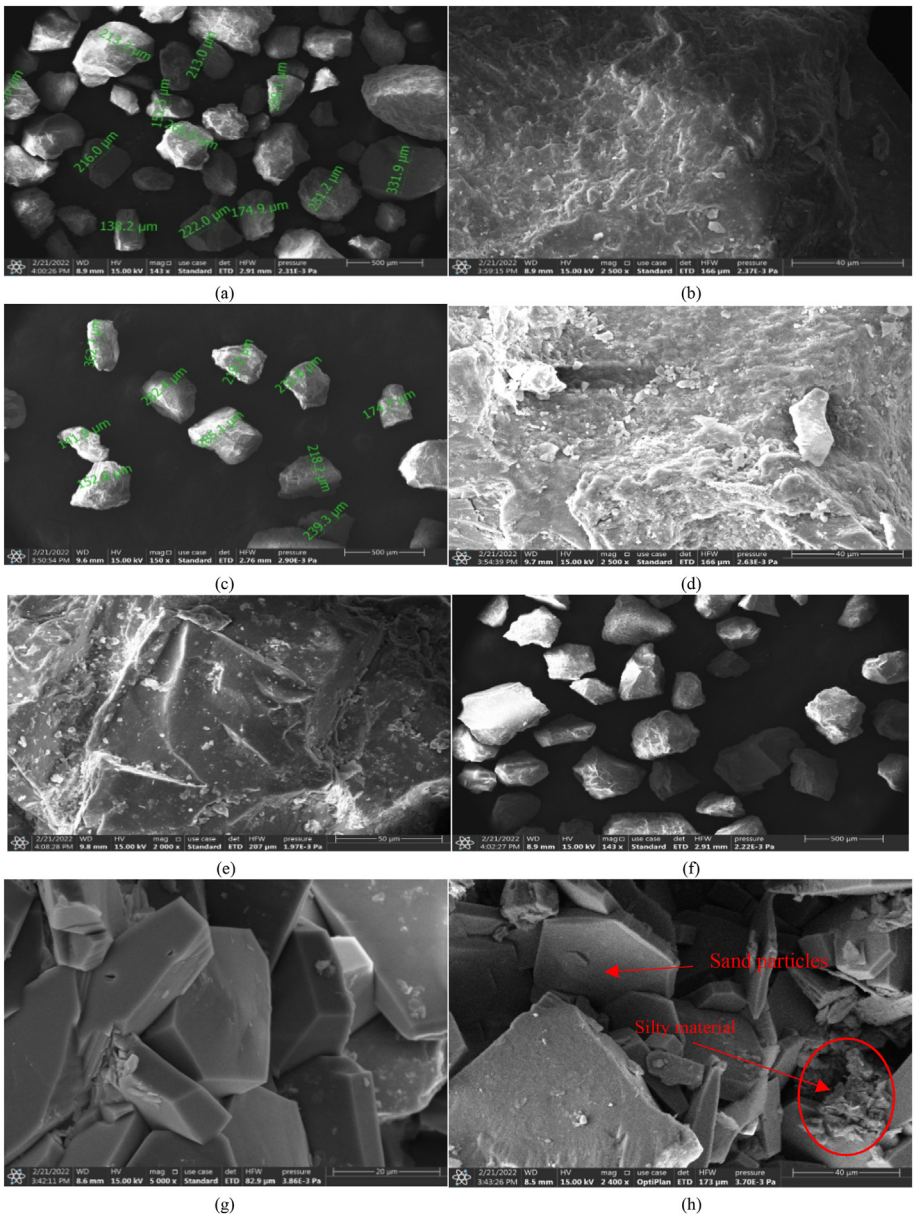

Fig. 22. Micro-characterization of the stratified specimen with silt thicknesses: (a) and (b) 14 mm; (c) and (d) 28 mm; (e) and (f) 42 mm; (g) and (h) 56 mm located at the middle of the specimen.

regression model (Eq. (10)) where the vulnerability decreases with an increase in the placement depth of silt layer.

3.9. Variation in shear modulus of the stratified specimens at different silt thicknesses

The presence of silty zone in a stratified specimen causes significant changes in the permeability of the whole specimen.

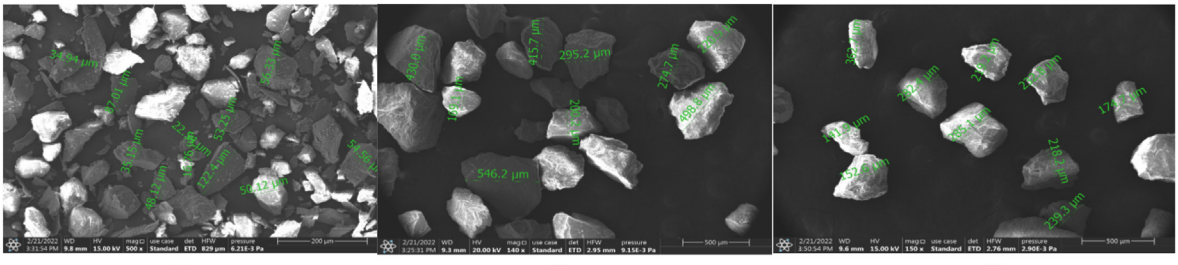

Fig. 23. SEM images for the specimen with silt layer at different locations (a) Top; (b) Middle; and (c) Bottom.

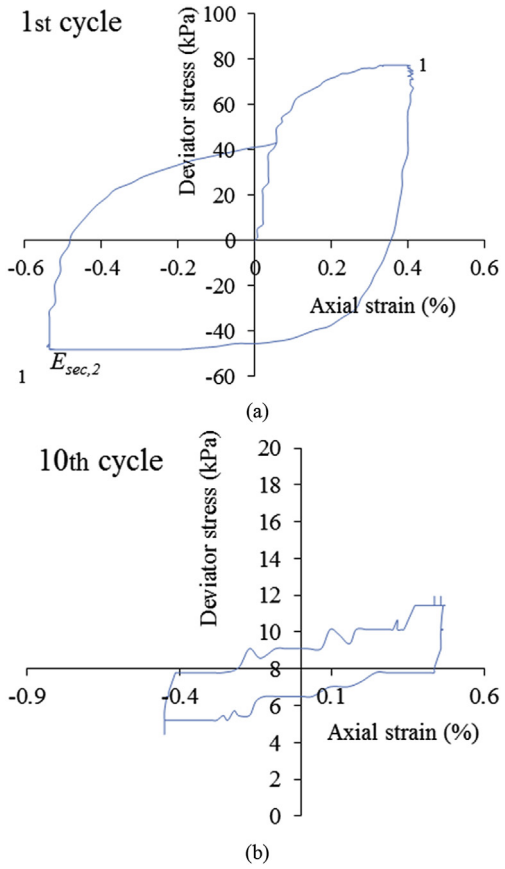

Fig. 24. Deviatoric stress versus strain plot for Specimen S5 (a) 1st cycle and (b) 10th cycle.

Therefore, localized pore pressure develops nearby the sand-silt interface. The changes in shear modulus (G) indicate the degradation of the soil specimen. Strain-controlled tests have been performed for calculation of the shear modulus of stratified specimens (Table 2). The strain-controlled undrained cyclic triaxial tests were performed at a strain rate of 0.4% at effective confining stress of 100 kPa. Shear modulus is directly correlated with the shear wave velocity of the soil specimen (Kramer, 1996). The comparison of the present study has been made with curves of Seed and Idriss (1970) for G/G_{max} values. G_{max} was calculated using Eq. (11) suggested by Seed and Idriss (1970). Elastic secant modulus has been calculated using Eq. (12). The maximum shear modulus was calculated as

$$G_{max} = 1000K_{2,max}(\sigma_m)^{1/2} \tag{11}$$

where $K_{2,max}$ is dependent on the soil relative density or void ratio, and σ'_m is the mean effective stress.

The maximum shear modulus for Solani River sand was 69 MPa. The shear modulus (G) has been calculated using the shear stress and shear strains obtained through the applied cyclic loadings using Eq. (13) (Kumar et al., 2017). The shear strain has been evaluated using Eq. (14) with the help of the axial strain values. A brief representation of stress-strain curve is presented using Fig. 24a for the stratified specimen S5 (silt thickness of 14 mm). It can be seen that a significant stiffness degradation has occurred till 10th cycles (Fig. 24b):

$$E_{sec} = \frac{E_{sec,1} + E_{sec,2}}{2} \tag{12}$$

$$G = \frac{E_{sec}}{2(1+\nu)} \tag{13}$$

$$\gamma = (1+\nu)\varepsilon \tag{14}$$

where E_{sec} is the secant elastic modulus, ν is the Poisson's ratio (for undrained cases taken as 0.5 by Rollins et al., 1998), γ is the shear strain, and ε is the axial strain.

Fig. 25 shows the data points of the stratified specimens for different silt thicknesses and the comparison with the upper and lower bound curves of Seed and Idriss (1970). The data points of optimum silt thickness (0.2 H or 28 mm) are located at the uppermost position. The reason behind this phenomenon is the minimal development of localized excess pore pressure in specimen S6. Specimen S8 with a silt thickness of 56 mm was found to have the least stiffness of the soil skeleton (see Fig. 25). The mechanism can be understood through Fig. 4b, where a large amount of localized pore pressure developed nearby silt layer. This was in agreement with the bulging images also (Fig. 5).

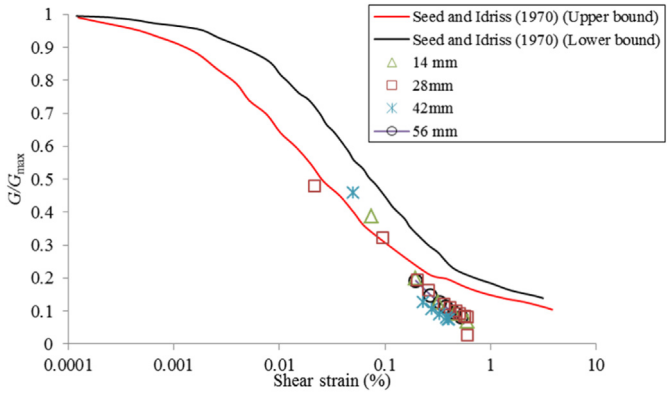

Fig. 25. G/G_{max} variation for the stratified specimen at different silt thicknesses.

4. Conclusions

In this study, consolidated cyclic triaxial tests were performed on both homogeneous and stratified specimens under undrained conditions. The testing materials were using Solani River sand and silt at different CSRs. The characteristics of the silt layer, i.e. thickness, location and number of silt layers, were assumed as the key parameters in governing liquefaction potential. On the basis of the results obtained, the following conclusions can be made:

(1) Stratified specimens with four different silt layer thicknesses and the specimens of homogeneous fine sand and silt were utilized in the cyclic triaxial tests. Remarkably, there exists an optimum silt layer thickness of 0.2H, at which liquefaction resistance was highest for CSR of 0.14. Additionally, after increasing the CSR from 0.14 to 0.26, a minimum effect of silt thickness increment was observed in governing liquefaction resistance due to the higher development rate of excess pore water pressure.

(2) The hindrance in pore-water flow due to the geology of the silt layer was found to be responsible for the development of localized pore pressure and localized bulging inside the vulnerable sandy zones. Failure cracks of about 2–3 cm were observed in the failed specimens.

(3) After considering optimum silt thickness as 0.2H, the silt layer was placed at three locations, i.e. top, middle and bottom. The capped soil condition (silt layer at top) appeared to be the most vulnerable where the specimen failed in 77 cycles. With an increase in the number of silt layers from single to double or triple, a lower amount of excess pore water migrated from the contractive zone to the dilative zone, which enhanced $N_{cyc,L}$ value to 560 at three silt layers ensuring significant liquefaction resistance.
(4) The relative firmness of sand-silt strata performed remarkably in governing the liquefaction susceptibility where the specimen with having sand and silt layer at relative densities of 50.48% and 72.85%, respectively, was found to be the most stable.
(5) A multi-linear regression analysis was performed after incorporating useful functions i.e. $F(CSR)$, $F(D_{r,m})$, $F(t)$, $F(z)$ and $F(n)$ for calculation of the number failure cycles to attain liquefaction ($N_{cyc,L}$). The adequacy of the developed model has been checked using the previous study with $R^2 = 0.98$, which depicts a strong correlation and validation of the present study.
(6) The observation from the micro-characterization suggested that the amount of silt content transported under the action of dissipated pore pressures. A clear difference in silt content was visible with changes in silt thickness and silt layer location. Also, the shear modulus calculation suggested that the stiffness degradation was highest in the specimen with a silt thickness of 56 mm.

Further studies can be performed on the silt interlayered sand specimens using numerical or analytical constitutive models, which may assist in developing an understanding of liquefaction vulnerable sites nearby alluvial plains, hydraulic fills and marine deposits.

Declaration of competing interest

The authors declare that they have no known competing financial interests or personal relationships that could have appeared to influence the work reported in this paper.

Acknowledgments

The experiments in this study have been performed at Geotechnical engineering lab, Indian Institute of Technology, Roorkee, India. Ministry of Human Resource Development, Government of India, New Delhi supported this work (Grant No. MHR 002).

Appendix A. Supplementary data

Supplementary data to this article can be found online at https://doi.org/10.1016/j.jrmge.2022.09.015.

List of notations and abbreviations

$N_{cyc,L}$	Number of cycles to attain liquefaction
e^*	Equivalent void ratio
D_r	Relative density
CSR	Cyclic stress ratio
FL	Failure line
PTL	Phase transformation line
$D_{r,m}$	Modified relative density
$D_{r,sand1}$	Relative density sand layer at upper location
$D_{r,sand2}$	Relative density sand layer at lower location
$D_{r,silt}$	Relative density of silt layer
n	Number of silt layers
P'	Mean effective stress
t_{conso}	Time required for consolidation (min)
t	Thickness of the silt layer
$e_{max,m}$	Maximum void ratio (modified)
$e_{min,m}$	Minimum void ratio (modified)
$R_{m,i}$	Percentage of the dry weight of ith layer
t_{opt}	Optimum silt layer thickness
q_{cyc}	Cyclic deviatoric stress
r_u	Excess pore pressure ratio
σ_c'	Effective confining stress
u	Pore pressure
H	Specimen height
z	Location of silt layer measured from the top
B	Skempton's pore pressure coefficient

References

Akçar, N., Yavuz, V., Ivy-Ochs, S., et al., 2019. Liquefaction of freshwater carbonates led to the February 10, 2011, landslide at the Çöllolar coalfield, eastern Turkey. Geomorphology 347, 106859.
Andrews, D.C.A., Martin, G.R., 2000. Criteria for liquefaction of silty soils. In: Proceedings of the 12th World Conference on Earthquake Engineering. New Zealand.
Arulanandan, K., Scott, R.F., 1993. Verification of numerical procedure for the analysis of liquefaction problems. In: Arulanandan, K., Scott, R.F. (Eds.), Conference Proceedings, 1. Balkema, Davis, CA.
ASTM D5311M-13, 2013. Standard Method for Load Controlled Cyclic Triaxial Strength of Soil. ASTM International, West Conshohocken, PA, USA.
Balakrishnan, A., Kutter, B.L., 1999. Settlement, sliding and liquefaction remediation of layered soil. J. Geotech. Geoenviron. Eng. 125 (11), 968–978.
Brennan, A.J., Madabhushi, S.P.G., 2005. Liquefaction and drainage in stratified soil. J. Geotech. Geoenviron. Eng. 131 (7), 876–884.
Bucci, M.G., Almond, P.C., Villamor, P., et al., 2018. Controls on patterns of liquefaction in a coastal dune environment, Christchurch, New Zealand. Sediment. Geol. 377, 17–33.
Ecemis, N., 2021. Experimental and numerical modeling on the liquefaction potential and ground settlement of silt-interlayered stratified sands. Soil Dynam. Earthq. Eng. 144, 106691.
Elgamal, A.W., Dobry, R., Adalier, K., 1989. Small scale shaking table tests of saturated layered sand-silt deposits. In: 2nd U.S.-Japan Workshop on Soil Liquefaction, 89-0032. Buffalo NCEER, Rep., pp. 233–245
Erdoğan, D.Ş., Tanrınian, N., Sezer, A., Karakan, E., 2020. Modelling results of liquefaction tests on a nonplastic silt. Mühendislik ve Yer Bilimleri Dergisi 5 (2), 96–122 (in Turkish).
Fiegel, G.L., Kutter, B.L., 1994. Liquefaction mechanism for layered soils. J. Geotech. Eng. 120 (4), 737–755.
Ghadr, S., Assadi-Langroudi, A., 2019. Effect of grain size and shape on undrained behaviour of sands. Int. J. Geosynth. Ground Eng. 5, 18.
Guan, Z., Wang, Y., Zhao, T.Y., 2022. Adaptive sampling strategy for characterizing spatial distribution of soil liquefaction potential using cone penetration test. J. Rock Mech. Geotech. Eng. 14 (4), 1221–1231.
Hussain, H., Sachan, A., 2019. Dynamic characteristics of natural Kutch sandy soils. Soil Dynam. Earthq. Eng. 125, 101517.
IS 2720-4, 1985. Methods of Test for Soils – Part 4: Grain Size Analysis. Bureau of Indian Standards, New Delhi, India.
Jain, A., Mittal, S., Shukla, S.K., 2021. Effect of specimen preparation technique on the post-liquefaction behaviour of fine sand under cyclic loading. Indian Geotech. J. 51, 1026–1037.
Jain, A., Mittal, S., Shukla, S.K., 2022. Cyclic behaviour of stratified soils under liquefied states. Mar. Georesour. Geotechnol. https://doi.org/10.1080/1064119X.2022.2095946.
Jia, M., Bingye, W., 2012. Liquefaction testing of stratified sands interlayered with silt. Appl. Mech. Mater. 256-259, 116–119.
Karakan, E., Altun, S., 2018. Determination of the cyclic properties of silty sands. In: Handbook of Research on Trends and Digital Advances in Engineering Geology. Balikesir University, Turkey.
Karakan, E., Sezer, A., Tanrinian, N., 2019a. Evaluation of effect of limited pore water pressure development on cyclic behavior of a nonplastic silt. Soils Found. 59, 1302–1312.
Karakan, E., Tanrinian, T., Sezer, A., 2019b. Cyclic undrained behavior and post liquefaction settlement of a nonplastic silt. Soil Dynam. Earthq. Eng. 120, 214–227.
Kirar, B., Maheshwari, B.K., 2018. Dynamic properties of soils at large strains in Roorkee region using field and laboratory tests. Indian Geotech. J. 48, 125–141.
Kokusho, T., Fujita, K., 2001. Water films involved in postliquefaction flow failure in Niigata City during the 1964 Niigata earthquake. In: Fourth Int. Conf. On Recent

Advances in Geotechnical Earthquake Engineering and Soil Dynamics 2001. University of Missouri-Rolla, Rolla.
Kokusho, T., Kojima, T., 2002. Mechanism for postliquefaction water film generation in layered sand. J. Geotech. Eng. 128 (2), 129–137.
Konrad, J.M., Dubeau, S., 2003. Cyclic strength of stratified soil samples. In: Locat, J., Mienert, J., Boisvert, L. (Eds.), Submarine Mass Movements and Their Consequences. Advances in Natural and Technological Hazards Research. Springer, Dordrecht.
Kramer, S.L., 1996. Geotechnical Earthquake Engineering. Pearson Education India.
Kulasingam, R., Malvick, E.J., Boulanger, R.W., Kutter, B.L., 2004. Strength loss and localization at silt interlayers in slopes of liquefied sand. J. Geotech. Geoenviron. Eng. 130 (11), 1192–1202.
Kumar, S.S., Krishna, A.M., Dey, A., 2017. High strain dynamic properties of perfectly dry and saturated cohesionless soil. Indian Geotech. J. 48 (3), 549–557.
Kumar, S.S., Krishna, A.M., Dey, A., 2018. Dynamic properties and liquefaction behaviour of cohesive soil in northeast India under staged cyclic loading. J. Rock Mech. Geotech. Eng. 10 (5), 958–967.
Lee, C.J., Chen, H.T., Lien, H.C., Wei, Y.C., Hung, W.Y., 2014. Centrifuge modeling of the seismic responses of sand deposits with an intra-silt layer. Soil Dynam. Earthq. Eng. 65, 72–88.
Liu, H., Qiao, T., 1984. Liquefaction potential of saturated sand deposits underlying foundation of the structure. In: Proceedings of the 8th World Conference on Earthquake Engineering, pp. 21–28. San Francisco, CA.
Maharjan, M., Takahashi, A., 2013. Centrifuge model tests on liquefaction-induced settlement and pore water migration in non-homogeneous soil deposits. Soil Dynam. Earthq. Eng. 55, 161–169.
Malvick, E.J., Kutter, B.L., Boulanger, R.W., Kabasawa, K., Kokusho, T., 2005. Void redistribution research with 1-g and centrifuge modeling. In: Proceedings of the 16th International Conference on Soil Mechanics and Geotechnical Engineering. Osaka, Japan.
Markham, C.S., Bray, J.D., Cubrinovski, M., Riemer, M.F., 2018. Liquefaction resistance and steady-state characterization of shallow soils within the christchurch central business district. J. Geotech. Geoenviron. Eng. 144 (6), 04018032.
Monkul, M.M., Kendir, S.B., Tütüncü, Y.E., 2021. Combined effect of fines content and uniformity coefficient on cyclic liquefaction resistance of silty sands. Soil Dynam. Earthq. Eng. 151, 106999.
Ni, X.Q., Zhang, Z., Ye, B., Zhang, S., 2022. Unique relation between pore water pressure generated at the first loading cycle and liquefaction resistance. Eng. Geol. 296, 106476.
Norini, G., 2021. Assessment of liquefaction potential in the central Po plain from integrated geomorphological, stratigraphic and geotechnical analysis. Eng. Geol. 282, 105997.
Özener, P.T., Ozaydin, K., Berilgen, M.M., 2009. Investigation of liquefaction and pore water pressure development in layered sands. Bull. Earthq. Eng. 7, 199–219.
Rollins, K.M., Evans, M.D., Diehl, N.B., Daily, W.D., 1998. Shear modulus and damping relationships for gravels. J. Geotech. Geoenviron. Eng. 124 (5), 396–405.
Seed, H.B., Lee, K.L., 1966. Liquefaction of saturated sands during cyclic loading. J. Soil Mech. Found Div. 92 (6), 105–134.
Seed, H.B., Idriss, I.M., 1970. Soil moduli and damping factors for dynamic response analyses. In: Rep. No. EERC70-10. College of Engineering, University. of California, Berkeley, CA.
Singh, S., 1996. Liquefaction characteristics of silts. Geotech. Geol. Eng. 14, 1–19.
Tasiopoulou, P., Giannakou, A., Chacko, J., Wit, S.D., 2019. Liquefaction triggering and post-liquefaction deformation of laminated deposits. Soil Dynam. Earthq. Eng. 124, 330–344.
Vaid, Y.P., Stedman, J.D., Sivathayalan, S., 2001. Confining stress and static shear stress in cyclic liquefaction. Can. Geotech. J. 38, 580–591.
Wang, Y., Wang, Y.L., Kong, L.W., Sun, Z.L., 2020. Post-liquefaction shearing behaviour of saturated gravelly soils: experimental study and discrete element simulation. J. Rock Mech. Geotech. Eng. 12 (1119), 1130.
Woźniak, P.P., Belzyt, S., Pisarska-Jamroży, M., et al., 2021. Liquefaction and re-liquefaction of sediments induced by uneven loading and glacigenic earthquakes: implications of results from the Latvian Baltic Sea coast. Sediment. Geol. 421, 105944.
Xiu, Z.g., Wang, S.H., Ji, Y.C., Wang, F.L., Ren, F.Y., 2019. Experimental investigation on liquefaction and post-liquefaction deformation of stratified saturated sand under cyclic loading. Bull. Eng. Geol. Environ. 79, 2313–2324.
Xu, G.H., Liu, Z.Q., Sun, Y.F., Wang, X., Lin, L., Ren, Y.P., 2016. Experimental characterization of storm liquefaction deposits sequences. Mar. Geol. 382, 191–199.
Xu, C.S., Feng, C.Q., Du, X.L., Zhang, X.L., 2020. Study on liquefaction mechanism of saturated sand considering stress redistribution. Eng. Geol. 264, 105302.
Yamaguchi, A., Kazama, M., Toyota, H., Kitazume, M., Sugano, T., 2002. Effects of the stiffness of soft clay layer on strong motion response. Soils Found. 42 (1), 17–33.
Yoshimine, M., Koike, R., 2005. Liquefaction of clean sand with stratified structure due to segregation of particle size. Soils Found. 45 (4), 89–98.
Zhang, J.L., Yang, Z.Y., Yang, Q., Li, G., Liu, J., 2021. Pore water pressure model for sands reinforced with randomly distributed fibers based on cyclic triaxial tests. Soil Dynam. Earthq. Eng. 148, 106812.

Arpit Jain is currently a PhD candidate at the Indian Institute of Technology, India. He is working on the dynamic behavior of stratified soil systems under the guidance of Prof. Satyendra Mittal and Prof. Sanjay Kumar Shukla. His research aligns with the high strain elements tests using cyclic triaxial and model tests based on a shaking table. Additionally, he has performed extensive tests to study sand boiling and water film formation in the stratified soil system. Apart from experimental testing, his study also considers numerical simulation using finite element software. He has worked on the areas of specimen preparation effect, post-liquefaction and utilization of waste material in geotechnical engineering.